https://doi.org/10.5194/essd-2019-155
Preprint. Discussion started: 11 October 2019

Open Access Earth System Science Data Discussions

A combined Terra and Aqua MODIS land surface temperature and meteorological station data product for China from 2003–2017

Bing Zhao[1,†], Kebiao Mao [2,3,†], Yulin Cai [1], Jiancheng Shi[4], Zhaoliang Li[3], Zhihao Qin[3], and Xiangjin Meng[5]

[1]Geomatics College, Shandong University of Science and Technology, Qingdao, 266590, China
[2]School of Geography, South China Normal University, Guangzhou 510631, China;
[3]Institute of Agricultural Resources and Regional Planning, Chinese Academy of Agricultural Sciences, Beijing, 100081, China;
[4]State Key Laboratory of Remote Sensing Science, Jointly Sponsored by the Institute of Remote Sensing Applications of Chinese Academy of Sciences and Beijing Normal University, Beijing, 100101,China;
[5]School of Surveying and Geo-Informatics, Shandong Jianzhu University, Jinan, 250100, China

*****Correspondence:* maokebiao@caas.cn; Tel.: +86-10-8210-8769.
†These authors contributed equally to this work and should be considered co-first authors.

Abstract. Land surface temperature (LST) is a key variable for high temperature and drought monitoring and climate and ecological environment research. Due to the sparse distribution of ground observation stations, thermal infrared remote sensing technology has become an important means of quickly obtaining ground temperatures over large areas. However, there are many missing and low-quality values in satellite-based LST data caused by cloud coverage exceeding 60 % of the global surface every day. This article presents a unique LST dataset in China for 2003-2017, which filters and removes missing values and poor-quality LST pixel values contaminated by clouds from raw LST images and retrieves real surface temperatures under cloud coverage by a reconstruction model. We specifically describe the reconstruction model, which uses a combination of MODIS daily data, monthly data and meteorological station data to reconstruct the true LST under cloud coverage, and then the data performance is further improved by establishing a regression analysis model. The validation indicates that the new LST dataset is highly consistent with the in situ observations. For the six natural subregions with different climatic conditions in China, the RMSE ranges from 1.24 °C to 1.58 °C, the MAE varies from 1.23 °C to 1.37 °C, and the R^2 ranges from 0.93 to 0.99. The new dataset adequately captures the spatiotemporal variations in LST at annual, seasonal and monthly scales. From 2003-2017, the overall annual mean LST in China shows a weak increase. Moreover, the warming trend was remarkably unevenly distributed over China. The most significant warming occurred in the central and western areas of the Inner Mongolia Plateau in the Northwest Region (slope>0.10, R>0.71, P<0.05), and a strong cooling trend was also observed in some parts of the Northeast Region. Seasonally, there was significant warming in the western part in winter, which was most pronounced in December. The reconstructed dataset exhibited significant improvements and can be used for the spatiotemporal evaluation of LST and high temperature and drought monitoring studies. The data are published in the Zenodo at https://doi.org/10.5281/zenodo.3378912 (Zhao et al., 2019).

https://doi.org/10.5194/essd-2019-155
Preprint. Discussion started: 11 October 2019

Open Access Earth System Science Data Discussions

1 Introduction

Land surface temperature (LST), which is controlled by land–atmosphere interactions and energy fluxes, is an essential parameter for the physical processes of the surface energy balance and water cycle at regional and global scales (Li et al., 2013; Wan et al., 2014; Benali et al., 2012). Accurate surface temperature datasets are not only required for high temperature and drought research over various spatial scales but also important elements for improving global hydrological and climate prediction models. In particular, temperature changes directly influence glacier reserves and water storage on the Qinghai-Tibet Plateau (Tibetan Plateau), which is known as the "World Water Tower". In turn, these changes directly affect the living conditions of nearly 40 % of the world's population (Xu et al., 2008). Therefore, LST research at regional and global scales is crucial for further improving and refining global hydroclimatic and climate prediction models. LST, which is conventionally measured by meteorological stations or ground surveys, has the advantages of high reliability and long time series. However, the meteorological station data collected as point data with very limited spatial coverage are often sparsely and/or irregularly distributed, especially in remote and rugged areas (Neteler, 2010; Hansen et al., 2010; Gao et al., 2018). To obtain spatially continuous LST data, various geostatistical interpolation approaches are commonly applied to achieve spatialization, such as kriging interpolation and spline function methods. However, the smoothed spatial pattern obtained after interpolation may suffer from low reliability because the ground station density is far from sufficient in most regions.

In contrast to the limited availability and discrete spatial information from ground-based observations, images captured by satellite thermal infrared instruments have become reliable alternative data sources with the advantages of detailed spatialized surfaces and near real-time data access (Vancutsem et al., 2010). For instance, for the study of uniform continuous surface temperatures over large-scale areas, such as over regional and global scales, satellite remote sensing is the only efficient and feasible method (Xu et al., 2013). Satellite remote sensing obtains global LST based on a variety of mature retrieval algorithms that have been proposed for use with data from thermal infrared channels, which dates back to the 1970s (McMillin, 1975). Due to the optimal temporal and spatial resolution throughout the world, the Moderate-resolution Imaging Spectroradiometer (MODIS) sensor has become an excellent data source for satellite-derived LST data and is widely used in regional and global climate change and environmental monitoring models (Tatem et al., 2004; Wan et al., 2014). However, satellite-derived LST data are frequently and strongly affected by cloud cover, causing many data gaps and a great deal of poor-quality values from undetected cloud contamination pixels. In fact, cloud cover is frequent, and the locations of cloud cover are often uncertain. On average, at any one time, approximately 65 % of the global surface is obscured by clouds, which directly leads to missing values over large, unevenly distributed areas in an image (Crosson et al., 2012; Mao et al., 2019). Although the integrity of the data has been greatly improved, the 8-day and monthly synthetic data still contain a number of low-quality pixels that are affected by the insufficient quantity of daily LST pixels. Cloud cover, which causes extensive amounts of missing and abnormal information, significantly reduces the usage rate of LST data and poses a problem to further applications. Thus, the reconstruction of noise-contaminated pixels, such as those contaminated by clouds, is necessary for LST applications.

https://doi.org/10.5194/essd-2019-155
Preprint. Discussion started: 11 October 2019

Two categories of methods have commonly been applied to reconstruct cloud contamination pixels from satellite-derived data in previous studies. The first category includes methods that directly reconstruct missing and poor-quality values using neighboring information with high similarity over temporal and spatial scales. Most temporal interpolation methods reconstruct missing and poor-quality values of LST data based on the periodic behavior of data, such as time series harmonic analysis (HANTS), S-G filtering, and Fourier transform (Xu and Shen, 2013; Na et al., 2014; Scharlemann et al., 2008). Crosson (2012) used another temporal interpolation method to reconstruct the LST data from the Aqua platform (afternoon overpass) using LST data from the Terra platform (morning overpass). Regarding spatial interpolation methods, previous methods have focused on geostatistical interpolation, including kriging interpolation, spline interpolation and their variants. Some researchers have also carried out other attempts; for example, Yu et al. (2015) introduced a method using a transfer function with the most similar pixels to estimate null pixels. These methods, which estimate missing MODIS LST data using only LST data, take advantage of the similarity and interdependence of the available temporal/spatial attributes of neighboring pixels. Thus, these methods have the advantage of simplicity and reliability. The second category of methods solves these data gap problems by establishing correlation models for cloud contamination pixels and corresponding auxiliary data pixels. Neteler (2010) used a digital elevation model (DEM) as an auxiliary predictor to reconstruct MODIS LST data from nine years of data on temperature gradients, which achieved reliable results in mountainous regions. Ke et al. (2013) built a regression model that included many auxiliary predictors—latitude, longitude, elevation, and the normalized difference vegetation index (NDVI)—to estimate 8-day composite LST products. Fan et al. (2014) used multiple auxiliary maps, including land cover, NDVI, and MODIS band 7, to reconstruct LST data in flat and relatively fragmented landscape regions. Other similar algorithms have drawn support by employing many factors that affect LST, including elevation, NDVI, solar radiation, land cover, distance from the ocean, slope and aspect. Considering the complexity of the terrain and the nonuniformity of the spatial distribution of large-scale LST patterns, a reconstruction model with auxiliary data that provides rich information for missing pixels can improve the accuracy of the interpolation result.

The above studies greatly improve the usability of MODIS LST data and further add value to long-term LST trend analyses. However, despite the use of various techniques to reconstruct the LST value, existing techniques focus on the retrieval of the LST value under the assumption of clear-sky conditions instead of cloudy conditions, which cannot fulfill the need to obtain the real situation at the land surface. To address this issue, some scholars have also used microwave temperature brightness (TB) data, which are mostly applied to high-frequency channels, to obtain the real LSTs under clouds (André et al., 2015; Prigent et al., 2016). Microwave remote sensing is capable of penetrating clouds and can obtain useful radiation information for the retrieval of LST under clouds. However, the physical mechanisms of the current microwave LST retrieval models are not very mature, and the models have low resolution (Mao et al. 2007, 2018). Moreover, due to the difference in the surface properties of the land, the depth of the radiation signal detected by the microwave will differ at different locations, and it will deviate from the retrieval results of thermal infrared remote sensing when used to estimate LST values. Thus, new reconstruction methods for LST data need to be proposed to compensate for this deficiency.

https://doi.org/10.5194/essd-2019-155
Preprint. Discussion started: 11 October 2019

On this premise, China is used as an example due to its large coverage area, heterogeneous landscape and complex climatic conditions. This paper presents a new long-term spatially and temporally continuous MODIS land surface temperature dataset in China from 2003 to 2017 that filters out missing and poor-quality pixels and reconstructs them based on multisource data. We describe a data reconstruction process that is fully integrated with the benefits of the high reliability of surface observations, consistency and high accuracy of daily valid pixels and spatial autocorrelation of similar pixels. The process compensates for the insufficiency of reconstructing pixels under clear-sky conditions instead of under clouds in previous studies. The validation using data from the China Meteorological Administration observations indicates the robustness of the LST data after interpolation. The dataset is ultimately used to capture the annual, seasonal and monthly spatiotemporal variations in the LST in six natural subregions of China. It is envisaged that this dataset will help capture the changes in surface temperature and will be useful for high temperature and drought studies and food security.

2 Study area

Insert Figure 1 here

Figure 1: The study area divided into six natural subregions (I, II, III, IV, V, VI), and the spatial patterns of the meteorological stations in the subregions. The red circles mark the key areas where the temperature changes significantly, and these areas are used to validate the accuracy of the new LST dataset (a, b, c, d, e, f).

Our study area of China is a large agricultural country, and its agricultural products are responsible for feeding more than 22 % of the world's population (Liu et al. 2004). However, agricultural production activities are very sensitive to climate change. In recent years, global warming has directly affected the crop growth system, which in turn has affected many aspects such as food production, food security, farmers' income and rural social and economic development. In addition, the Qinghai-Tibet Plateau, which is known as the “World Water Tower”, supplies water for life, agriculture, and industry for nearly 40 % of the world's population through extensive glacial snow (Xu et al., 2008, Gafurov and Bárdossy, 2009, United Nations Environment Programme (UNEP), 2007). In recent years, increasing temperatures have forced glaciers in many large mountains to melt at an accelerating rate (Oku et al., 2006). The water resources from the water tower will be rapidly reduced, which will bring a series of serious water and ecological security problems. Therefore, the generation of a complete set of datasets that reflect the spatiotemporal variations in temperature will be helpful to study the temperature changes in China, especially the Qinghai-Tibet Plateau, and will be of great significance to agricultural production and drinking water supplies in neighboring countries.

Therefore, to explore the temporal and spatial characteristics of China's LST, the study area is divided into six natural subregions based on China's three major geographical divisions, climatic conditions, landform types and tectonic movement characteristics. The eastern region is characterized by the topographical features of plains and low mountains. This region has a variety of monsoon climate zones, which travel from south to north and include tropical, subtropical and temperate monsoon climate zones. Therefore, we divide the eastern region into the following four regions, as shown in Fig. 1. (I) The

https://doi.org/10.5194/essd-2019-155
Preprint. Discussion started: 11 October 2019

Northeast Region, which mainly covers the area to the east of Daxing'anling. This region has a temperate monsoon climate with average annual precipitation of 400~1000 mm, and rain and heat are prevalent in the same period. This large vast plain (approximately 55.8 % of the land area in China) and good climatic conditions are very conducive to the growth of crops, making the Northeast Region one of China's most important grain-producing areas. (II) The North China Region includes the south of the Inner Mongolia Plateau, the north of the Qinling Mountains and Huaihe River, and the east of the Qinghai-Tibet Plateau. The region is dominated by a temperate monsoon climate and a temperate continental climate with four distinct seasons. This area is characterized by flat plains and plateau terrain. (III) The Central - South China Region that extends from the eastern part of the Qinghai-Tibet Plateau to the western parts of the East China Sea and South China Sea, south to the Huaihe River - Qinling Mountains, and north to the area where the daily average temperature is greater than or equal to 10 °C. The accumulated temperature in this region is 7500 °C. This region is commonly dominated by a subtropical monsoon climate. (IV) The South China Region is located in the southernmost part of China and is characterized by a tropical and subtropical monsoon climate with hot and humid conditions. The area has abundant rainfall, and the average annual precipitation is approximately 1900 mm.

The western region is divided into 2 natural subregions. (V) The Northwest Region, which includes the north of the Qilian Mountain-Altun Mountains-Kunlun Mountains, the Inner Mongolia Plateau and the western part of the Greater Khingan Range. This region is located inside the mainland with complex terrain conditions, and the topography is mostly plateau basins and mountainous areas. This region has a tropical dry continental climate with rare rainfall. This area has a wide range of barren land, with a desertified land area of 2.183 million km^2, accounting for 81.6 % of China's desertified land area (Deng, 2018). Moreover, the Taklimakan Desert in this region is one of the top ten deserts in the world. (VI) The Qinghai-Tibet Plateau Region is mainly located in the Qinghai-Tibet Plateau, which is the plateau with the highest altitude in the world. This region is mainly described to have an alpine plateau climate, with a relatively high temperature and a large grassland meadow.

3 Data and methods

3.1 MODIS data

MODIS is a key sensor that was launched by the Earth Observing System (EOS) program and provides a unified grid product with global coverage of the land, atmosphere and oceans. Because MODIS covers 36 spectral bands from the visible, near-infrared and thermal infrared ranges (from 0.4 to 14.4 mm), it is extensively used to study global marine, atmospheric, and terrestrial phenomena (Wan et al., 1997). The MODIS instruments are aboard two NASA satellites, Terra and Aqua, which were launched in December 1999 and May 2002, respectively. As both the Aqua and Terra satellites are near-polar orbit satellites with a flying height of approximately 705 km in sun-synchronous orbit, they provide data with a temporal resolution of twice daily. The Terra satellite passes through the equator from north to south at approximately 10:30 am and 10:30 pm local solar time and is called the morning star. However, the Aqua satellite passes through the equator in the

https://doi.org/10.5194/essd-2019-155
Preprint. Discussion started: 11 October 2019

opposite direction from south to north at approximately 1:30 am and 1:30 pm and is called the afternoon satellite (Christelle and Ceccato, 2010). The two satellites collect repeated observations every 1-2 days and transmit observation data to the ground in real time.

The MODIS LST is retrieved from two algorithms: the generalized split-window algorithm (Wan and Dozier, 1996; Wan et al., 2002) and the day/night algorithm (Wan and Li, 1997). The split-window algorithm is advantageous for removing atmospheric effects because the signal difference between the adjacent thermal and middle infrared channels (channel 31 with a wavelength of 10.78–11.28 μm and channel 32 with a wavelength of 11.77–12.27 μm) is caused by the differential absorption of radiation in the atmosphere (Wan et al., 2002). The latest LST V006 version data used in this article is obtained by another important algorithm: the day/night algorithm. Due to the complexity of surface reflectance and atmospheric conditions, multichannel data are utilized in day/night image pairs to derive the LST, including radiation calibration data, atmospheric temperature and water vapor data, cloud masks and geolocation information and L1B data in seven thermal infrared bands (bands 20, 22, 23, 29, 31, 32, 33) from MOD07_L2 (Wan, 2007). Then, these day/night pairs of MODIS data are used to construct a physics-based day/night LST model based on nonlinear equations of 14 thermal infrared observations to retrieve the surface average emissivity and surface temperature values from the MODIS LST product without high-accuracy atmospheric temperature and water vapor profiles (Wan and Li, 1997).

The day/night LST algorithm used in the LST V006 version products exhibits great advantages in retrieving LST: it not only optimizes atmospheric temperature and water vapor profile parameters for optimal retrieval but also does not require complete reversal of surface variables and atmospheric profiles (Ma et al., 2000, 2002). A comprehensive sensitivity and error analysis was performed for the day/night algorithm, which showed that the accuracy was very high, with an error of 1–2 K in most cases (0.4-0.5 K standard deviation over various surface temperatures for mid-latitude summer conditions) (Wan and Li, 1997, Wang and Liang, 2009; Wang et al., 2007).

Here, two MODIS products were chosen for research: daily LST data (MOD11C1 and MYD11C1) and monthly LST data (MOD11C3 and MYD11C3), which were available for the period from 2003–2017. The datasets include daytime and nighttime surface temperature data provided by NASA. These data are the new collection 6 series data provided in 2017, which has been fixed and substantially improved compared to the collection 5 data used in many previous studies. In collection 6 data, the identified cloud-contaminated LST pixels were removed from the MODIS Level 2 and Level 3 products, and the classification-based surface emissivity values were adjusted (Wan. 2014). Both datasets provide the global LSTs generated by the day/night algorithm with a spatial resolution of 0.05°×0.05° (approximately 5600 m at the equator), which is provided in an equal-area integerized sinusoidal projected coordinate system. The composited 8-day (MOD11C2/MYD11C2) and monthly (MOD11C3/MYD11C3) data are deduced from daily global data (MOD11C1/ MYD11C1) without cloud contamination. The global LST product MOD11C1/MYD11C1 (V006) was created by assembling daily MOD11B1/MYD11B1 tiles and resampling from 5600 m spatial resolution to a resolution of 7200 columns and 3600 rows of the latitude/longitude grid.

https://doi.org/10.5194/essd-2019-155
Preprint. Discussion started: 11 October 2019

The preprocessing of the MODIS data mainly includes extraction of daytime and nighttime LST and the corresponding quality assessment (QA) data from 17 scientific datasets, projection conversion (reprojection of raw data from a sinusoidal projection (SIN) to an equal-area conical projection (Albers), WGS84 coordinate system), conversion of the data format (conversion from HDF to Geo-tiff), and clipping (selection of geographic subsets according to latitude and longitude position to improve the efficiency of the model). The brightness temperature is converted to real surface temperature by coefficient and offset correction.

3.2 Supplementary data

The LST records in China for the hourly intervals from 2399 meteorological ground stations from 2003-2017 were used in this study, and they were provided and underwent strict quality control and evaluation by the China Meteorological Administration (CMA). Meteorological station data were randomly divided into two completely independent subsets by the jackknife method. Subset (1): the number of ground stations used for the reconstruction process was 1919, accounting for 80 % of the total number of ground stations. Subset (2): the number of sites used for verification was 480, accounting for 20 % of the total. Then, the data used for the reconstruction process in subset (1) were created by extracting meteorological station LST data at the overpass times of Terra and Aqua (01:30, 10:30, 13:30, and 22:30). For the verification process, six key areas where warming/cooling trends were the most significant (i.e., shown in the red ellipse a-f in Fig. 1 and Table 1) were selected for detailed verification to better reflect the accuracy of the LST data. All meteorological ground station data were tested for temporal and spatial consistency, which included identifying and rejecting extreme values and outliers.

Table 1 Basic information for some of the meteorological stations in key zones

Insert Table 1 here

Elevation data with 1 km resolution are available from the NASA Space Shuttle Radar Terrain Mission (SRTM) V4.1 for reconstruction of cloud-contaminated data.

3.3 LST data restoration method

For satellite-derived LST data, due to the extensive and random distribution of missing and unreliable values caused by cloud contamination in the images, it is difficult to reconstruct the operational LST dataset under clear-sky conditions and on a daily scale, and it is even more difficult to retrieve the LSTs to identify the real performance of the LST reconstruction under cloud coverage. Therefore, we create a reconstruction model that combines meteorological station data and daily and monthly MODIS LST data to reconstruct a high-precision dataset that can reflect the true LST under cloud coverage. The reconstruction model effectively preserves the highly accurate pixels in the original daily data, reconstructs only the poor-quality daily data, and finally, replaces low-quality pixels with the composite average pixel value in the monthly data. To better describe the data processing, Fig. 2 shows a summary flowchart for the reconstruction of MODIS monthly LST data. The reconstruction model we proposed is divided into two general steps: LST pixel filtering and LST data restoration. Contaminated pixel values were first identified and eliminated for all monthly LST images that were input based on pixel

https://doi.org/10.5194/essd-2019-155
Preprint. Discussion started: 11 October 2019

quality filtering. After the contaminated pixels were determined, we traversed the corresponding daily pixels and reconstructed the daily pixels with poor quality in the month. We reconstructed all contaminated daily pixels via three substeps: 1) the in situ LST observations at the same location, which was judged by the longitude and latitude information, were used to fill the contaminated pixels at the same location. 2) the geographically weighted regression (GWR) method was employed to interpolate contaminated pixels based on similar pixels from multiple sources. 3) the remaining contaminated pixels were reconstructed based on regression of the elevation temperature gradient. Finally, the averages of the available daily LST pixels were calculated and filled using the corresponding monthly pixels.

Insert Figure 2 here

Figure 2: The summary flowchart for reconstructing MODIS monthly LST data.

3.3.1 Filtering of MODIS LST

MODIS LST data are retrieved by a thermal infrared band in clear-sky conditions, which will contain many missing values and poor-quality values caused by clouds and other atmospheric disturbances. Generally, the cold top surface of a thin or subpixel cloud is difficult to detect, and the LST retrieved under such conditions usually leads to an underestimation of the temperature values in the MODIS LST data (Neteler, 2010; Markus, 2010; Jin and Dickinson, 2010; Benali et al., 2012). Moreover, other factors can also contaminate the observation signal and cause the data to be unavailable, such as atmospheric disturbance, variable illumination, observation geometry and instrumental problems (Wan, 2014). In general, the abnormally low values in LST maps caused by undetected thin clouds, together with other poor-quality values, need to be identified and filtered because these values greatly reduce the accuracy of the LST data.

Cloud cover is extensive and inevitable in daily weather conditions. Statistical calculations were performed, which showed that missing values for daily data reached approximately 50 % for Terra and Aqua satellites. Figure 3 shows an example representing the distribution of valid pixel values in the daytime for winter and summer. The coverage of pixels with missing data in the study area at 10:30 am during the daytime on January 1, 2017, and July 1, 2017, for the Terra platform reached 44.9 % and 51.7 %, respectively. The spatial gaps in the daily data are characterized by an arbitrary distribution and generally large aggregations. In fact, the emergence of a large number of missing values makes it difficult to reach a high-precision reconstruction result that represents real values under clouds using current techniques due to such a paucity of information, especially for areas with complex climates.

However, the random occurrence of cloud-covered areas has a much smaller impact on monthly composite products, which makes these products a reliable source for building a high-precision LST dataset. Compared with daily and 8-day composite data, spatiotemporal integrity and consistency have been greatly improved in monthly composite LST data. However, for many regions, the lack of data or quality degradation caused by clouds is still common even in monthly composite data. It is necessary to identify and reconstruct cloud-contaminated pixels, which seriously affect the use and analysis of data. A reliable method for removing the poor-quality pixels is implemented using the data quality control information for MODIS LST data. The data quality control information is statistically calculated and stored in the

https://doi.org/10.5194/essd-2019-155
Preprint. Discussion started: 11 October 2019

corresponding QA layer and is represented by an 8-bit unsigned integer and can be found in the original MODIS LST HDF files. Therefore, we use the quality control labels for daily and monthly files as mask layers to eliminate poor-quality pixels to ensure the quality of the LST data. Finally, pixels with QA layer labels of "the average LST error <=1 K", "LST produced, good quality" and "the average emissivity error <=0.01" are considered to be high-quality data, and the remaining pixel values are rejected. Quality information is almost indicative; thus, sufficient information is provided for the filtering of low-quality pixels (Benali et al., 2012). A summary flowchart of the process used to construct the LST data model is schematically illustrated in Fig. 2.

The spatial distribution pattern of invalid Terra LST data after filtering by the QA layer is shown in Fig. 4. The low-quality pixel coverage rates for January and July 2017 were 23.45 % and 19.68 %, respectively. There are more missing values in winter than in summer in the northeastern region, which may be affected by the confusion resulting from large areas of snow cover and clouds in the winter. However, the missing values are mainly concentrated in southern China in summer, which is closely related to the increased cloud cover in the hot summers in South China.

Insert Figure 3 here

Figure 3: Spatial distribution of valid data for daily MODIS LST data from Terra at 10:30 am (a) January 1, 2017, and (b) July 1, 2017. Areas of invalid data are in white.

Insert Figure 4 here

Figure 4: Spatial distribution of valid data for monthly MODIS LST data from Terra at 10:30 am in (a) January and (b) July. Areas of invalid data are in white.

3.3.2 LST data restoration

Missing values caused by cloud coverage have always been an important limitation of using LST from thermal infrared (TIR) data in a wide range of applications. For daily LST data, although many attempts have been made to reconstruct the LST data under clear-sky conditions, the widespread missing values make it difficult to reconstruct high-precision real LST values under clouds using the limited available information. To obtain a high-precision LST dataset that could retrieve the true temperature of the land surface under cloud cover instead of clear skies, we adopted another strategy to reconstruct the high-precision LST dataset.

Given that monthly LST data are composited from the corresponding daily data, an insufficient amount of valid daily data and low availability for some pixels will lead to quality degradation in the monthly data. The contributions of multiple valid daily pixels $\bar{P}_i$, despite their good precision, are rejected along with the final poor-quality values in monthly pixels. Thus, considering the inheritance of these high-quality data, we believe that these valid daily pixels $\bar{P}_i$ can help to reconstruct high-precision estimates for LST pixels under cloudy conditions. Therefore, in the reconstruction model, we first filter the monthly image, and the locations of the pixels that are contaminated by clouds (i.e., the missing and poor-quality monthly pixels) are determined. Then, we filter all the daily pixels for the month when the cloud-contaminated pixels occurred. The valid pixels $\bar{P}_i$ in the daily data are retained, the poor-quality daily data are reconstructed, and the low-quality pixels in the

https://doi.org/10.5194/essd-2019-155
Preprint. Discussion started: 11 October 2019

monthly data are replaced with the corresponding averaged pixel values from the daily data (Fig. 2). The reconstruction process for the cloud-contaminated daily pixels, which are defined as the target pixels, is as follows.

The real ground LST values in pixels obscured by clouds are usually lower than the values in the adjacent unaffected pixels, and the ground meteorological station values observed at the same time as the prediction result are the most reliable among all predictor factors, such as NDVI, longitude and latitude. Therefore, the latitude and longitude information of the target pixels was first used to search for the ground stations in the same location. Target pixels were filled using the values from valid ground-based LST data at the same location at the same time, and these filled pixels were marked. Then, for the target pixels without ground meteorological station data, we used a combination of two strategies to reconstruct the missing LST data to improve the accuracy of the result. The first strategy identified the most similar pixels by using adaptive thresholds and reconstructed them by using a GWR method.

GWR is a common and reliable method for estimating missing pixels, which quantifies the contribution of each similar pixel to contaminated pixels. This method assumes that similar pixels that are spatially adjacent to the target pixel are close in the spectrum and should be given more weight. Therefore, the GWR method can be represented as follows

$$T = \sum_{i=1}^{n} W_i \cdot T_i \ , \quad (1)$$

where T is the reconstructed LST value of a target pixel, T_i is the value for the similar pixel i, W_i is the weight coefficient, and the sum of all W_i values is 1.

Due to the high temporal variability of thermal radiation emitted from the land surface and atmospheric state parameters, satellite sensors that measure the thermal radiation energy from different phase images at the same locations often produce different values even when the same thermal infrared sensor is used. Some of the most common regular changes in surface features, such as the vegetation spectrum changes due to seasonal changes, can be predicted using auxiliary information. However, multiple unpredictable changes that cause abrupt transformation in the thermal energy of infrared radiation are difficult to predict, such as wheat harvesting and the expansion of a city. Therefore, it is only possible to determine the most accurate similarity relationship for the target pixels by selecting the image from the nearest phase. Thus, for the target pixel i and a valid pixel j in the same image, the three images that are temporally closest at the same overpass time are determined as reference images, and a threshold is then used in the reference image to determine whether the pixels corresponding to pixels i and j are similar. If two pixels are judged to be similar in more than one image, the valid pixel j is identified as a similar pixel for the target pixel i.

As the factors that influence surface temperature (vegetation cover, sun zenith angle, microrelief, etc.) vary greatly in different regions and seasons, the spectral differences of adjacent pixels in different areas may also vary greatly. Thus, there will be large deviations in the similar pixel decision criteria if a fixed similarity threshold is used. Here, we use an adaptive threshold φ^{τ} , which denotes the smoothness of the local area, to determine similar pixels for each null pixel (Eq. 3). For the jth valid pixel in the target image, it is determined to be a similar pixel of the target pixel i only when the relationship described in Eq. (2) is satisfied in the reference image τ. Simultaneously, similar pixels were determined based on all valid

https://doi.org/10.5194/essd-2019-155
Preprint. Discussion started: 11 October 2019

pixels in the image rather than a sliding window because missing values are often arbitrarily clustered in a large area rather than scattered.

$$|P_s^\tau - P_t^\tau| \le \varphi^\tau \,, \tag{2}$$

$$\varphi^\tau = \sqrt{\sum_{i=1}^{n}(P_s^\tau - \varepsilon)^2}, \tag{3}$$

Where P_s^τ and P_t^τ are the values of pixels corresponding to the position of the similar pixel and the target pixel in the reference image, respectively. φ^τ is the threshold used to determine similar pixels. ε is the mean value of the local pixels. τ is the reference image (value=1, 2, 3). Here, we set the range of the local area to 5 pixels by 5 pixels (Zeng et al., 2013). In this paper, the number of similar pixels should be greater than 4 to apply the GWR method to reduce the error due to an insufficient number of similar pixels.

After determining similar pixels, the LST values of the pixels contaminated by clouds are determined through GWR. In theory, LST data from meteorological stations are the most reliable record, even in the case of thick cloud coverage. Thus, similar pixels obtained from ground stations are the most representative, which can better reflect the LST under clouds than in clear-sky conditions. In the process of reconstructing missing pixels, we assign a related weight multiplier to the marked ground station data based on the GWR. After selecting some of the marked pixels as experiments, it was found that the target pixels could be more accurately estimated when the relative multiweight values of the ground stations were set to 3 in this paper. Therefore, the weighting coefficients of similar pixels are determined by Eqs. (5) and (6).

$$D = \sqrt{(x - x_t)^2 + (y - y_t)^2}, \tag{4}$$

$$W_i = \frac{\frac{M_c}{D_i}}{\sum_{i=1}^{m}\frac{M_c}{D_i} + \sum_{j=1}^{n}\frac{M_g}{D_j}}, \tag{5}$$

$$W_j = \frac{\frac{M_g}{D_j}}{\sum_{i=1}^{m}\frac{M_c}{D_i} + \sum_{j=1}^{n}\frac{M_g}{D_j}}, \tag{6}$$

where D represents the distance from the similar pixel to the target pixel t, x, y, x_t and y_t describe the locations of the similar pixel and target pixel. i and j represent similar pixels used to estimate the poor-quality LSTs, i is a pixel that is not contaminated by clouds, and j is a pixel assigned by the ground station. W_i and W_j describe the weight that similar pixels i and j contribute to the target pixels, respectively. m is the number of similar pixels that are not contaminated by clouds, and n is the number of similar pixels that are assigned by ground stations. M_c and M_g represent the weight coefficients of cloudless contaminated pixels and ground station assignment pixels, respectively. In this paper, M_c and M_g are set at 1 and 3, respectively.

For another strategy, the elevation temperature gradient regression method was used to reconstruct the remaining contaminated pixels that did not have enough similar pixels. In general, the elevation factor has a particularly significant effect on the spatial variation at the regional scale. Elevation is recognized as the most important factor that characterizes the overall spatial trend of LST (Sun, 2016). DEM data and LST data are used to construct linear regression relationships for

https://doi.org/10.5194/essd-2019-155
Preprint. Discussion started: 11 October 2019

null pixels based on the nonempty pixels in the neighborhood of a certain window size; these data are then used to predict the missing value pixels by linear interpolation. After several simulations of the experimental pixel window size, the noise was found to be minimized when a sliding window of 19 by 19 pixels was used, and this window size was considered to have the best complement value.

$$T_i = \alpha \times h_i + \beta, \quad (7)$$

where T_i is the surface temperature data after interpolation (units: °C); h_i is the elevation value of pixel i (units: m); α is the influence coefficient of the elevation on the surface temperature, which is the regression coefficient; β is the estimated intercept. Finally, we accurately crop the image to a Chinese-wide image to ensure that the sliding pixel window reaches the edge of the study area.

3.4 Analysis of the LST time series trend

In this study, the slope of a linear regression describes the rate of LST cooling/warming, which is calculated by Eq. (8). The slope value and correlation coefficient (R) were selected to quantify the temporal and spatial patterns in the LST variations using Eq. (9).

$$Slope = \frac{\sum_{i=1}^{n}(iT_i) - \frac{1}{n}\sum_{i=1}^{n} i \sum_{i=1}^{n} T_i}{\sum_{i=1}^{n} i^2 - \frac{1}{n}(\sum_{i=1}^{n} i)^2}, \quad (8)$$

$$R = \frac{n\sum_{i=1}^{n}(iT_i) - \sum_{i=1}^{n} i \sum_{i=1}^{n} T_i}{\sqrt{n\sum_{i=1}^{n} i^2 - (\sum_{i=1}^{n} i)^2}\sqrt{n\sum_{i=1}^{n} T_i{}^2 - (\sum_{i=1}^{n} T_i)^2}}, \quad (9)$$

where i is the number of years, T_i is the average LST of year i, and n is the length of the LST image time series; here, n is 15. When slope>0, it indicates that LST shows a warming trend. When slope<0, it indicates that the surface temperature is cooling. The R values range from -1 to 1. An R value greater than 0 means that the LST is positively correlated with the time series, and an R value less than 0 means that the LST is negatively correlated with the time series. Meanwhile, the larger the absolute value of R is, the stronger the correlation with the time series changes.

4 Results

Temperature changes show significant differences at different time scales (day, night, month, season and year) and different spatial scales. Therefore, various QA methods were performed to validate the new data on the monthly and seasonal scales. Furthermore, to better understand the spatial and temporal variations in surface temperature and the reactions of different regions, we analyze the LST at yearly, seasonal and monthly scales and show the changes in temperature during the day and at night.

https://doi.org/10.5194/essd-2019-155
Preprint. Discussion started: 11 October 2019

4.1 Annual change analysis

4.1.1 Average change

To obtain the overall LST trend, we averaged the LST for each year to remove seasonal effects. Fig. 5 shows the annual average LST change in China over the period from 2003-2017. The LST fluctuations in China exhibited a general weak warming trend. The sliding average of the 5-year unit also showed a weakly fluctuating warming trend. The lowest LST in China appeared in 2012 at 7.51 °C. The temperature reached its highest value in 2007 (9.25 °C), but after 2012, the LST remained high. This result coincides with the global warming stagnation period that was noticed from 1998-2012, and the LST increased significantly after 2012. After analyzing the LST on the seasonal and monthly scales, we found that the cooling in 2012 mainly occurred in the winter, as it was concentrated from January-February, and the cooling in the southern region was more significant than that in the other regions. In 2012, due to the abnormally strong East Asian winter monsoon, there was abnormal rainfall in the south in winter. We also observed a sudden decrease in LST in 2008 and a sudden increase in 2013. In 2008, severe persistent low-temperature snowstorm events in southern China in winter caused a decline in LST. The warming in 2013 was mainly affected by the abnormally high temperatures in the middle and lower reaches of the Yangtze River in summer.

Insert Figure 5 here

Figure 5: Annual mean LST changes in China from 2003 to 2017.

Insert Figure 6 here

Figure 6: Spatial dynamics of interannual change trends in LST from the slope (a) computed by Eq. (8), the correlation coefficient (b) computed by Eq. (9) and frequency distribution of the slope (c) during 2003-2017. In panel c, the different temperature trends (slope) are divided into 10 subinterval ranges corresponding to the ranges in panel a. The left side of the AB line represents the proportion of the area that experienced cooling, and the right side represents the proportion that experienced warming.

For a more detailed understanding of the spatial patterns and regional differences in the LST changes in different areas, the rate of annual average LST change per pixel from 2003 to 2017 was calculated, and the slope (Fig. 6a), correlation coefficient (Fig. 6b) and frequency distribution of the slope (Fig. 6c) are shown. From 2003-2017, the annual average LST in China showed a weakly positive trend. The LST exhibited a strong warming trend in many regions of the north but negative trends in the south, and the positive trend in the west was greater than that in the east. Different regions showed significant regional variations. Most of China experienced a warming trend (slope>0), which accounted for 63.7 % of the study area (which corresponds to the pale yellow, yellow, light orange, orange, and red parts in Fig. 6c). Additionally, approximately 20.80 % of the pixels underwent significant warming (slope>0.05, R>0.6). The areas with significant warming were mainly concentrated in the Mongolian Plateau and its southern areas in the northwestern region. In contrast, 36.25 % of the districts showed a cooling trend (slope<0, depicted in green and 4 shades of blue in Fig. 6c). The area with a significant cooling pattern (slope<-0.075, R>-0.6) covered 6.53 % of the study area, and these patterns were mainly concentrated in the northeast. The specific spatial variation characteristics of LST in different regions are summarized as follows.

https://doi.org/10.5194/essd-2019-155
Preprint. Discussion started: 11 October 2019

In 2013, the Intergovernmental Panel on Climate Change (IPCC) noted that climate warming is clear (IPCC et al., 2013). However, some areas of the Northeast Region (I) showed a significant warming hiatus over the past 15 years, and these areas made the greatest contribution to China's cooling trend. We observed widespread and relatively strong cooling regimes in most areas (i.e., the slope value ranged from -0.06 to less than -0.12, see Fig. 6a, b for details) except for the northeastern part of the Greater Xing'an Mountains. The cooling trend in Northeast China in recent years may be related to the negative Arctic oscillations in the northeast, which are closely related to the Siberian high (SH) and the East Asian Trough (EAT) during this period (Sun et al., 2017). Attention should be paid to the Northeast Plain because it is China's most important region for commercial grain (corn, rice) and cash crops (soybeans, sugar beets, etc.), accounting for approximately 15 % of the country's total grain production (Yang et al., 2007). Intensified cold conditions will cause insufficient accumulated temperature in the crop growth period, which will cause large-scale crop yield reductions. In addition, if this rapid cooling continues in the Northeast Region, it will pose a great threat to agricultural production and the development of the regional economy. The possible impacts should be brought to the attention of the relevant agricultural sector, and appropriate preventive and regulatory measures should be taken.

In the North China Region (II), we observed that the pattern of the spatial variations in LST has interesting characteristics: the trends were opposite on the two sides of the Taihang Mountains. There were warming trends in the western part of the Taihang Mountains but cooling trends in the eastern part of the Taihang Mountains. Furthermore, the western part of the Taihang Mountains is the Loess Plateau with a high elevation, and the eastern part is the North China Plain with a low elevation (Fig. 1). The North China Plain and the Yangtze River Delta in the south both exhibit obvious warming trends, both of which are densely populated areas. The relatively high warming trends may be attributed to the rapid increase in population and the generation of more greenhouse gas emissions during rapid urbanization in recent years. In addition, the Central China-Southwest Region (III) and the South China Region (IV) also showed negative trends, but the cooling trends were not significant.

In the Northwest Region (V), it was discerned that some area in Tianshan Mountains and the Inner Mongolia Plateau experienced significant warming trends (slope>0.10, R>0.71, P<0.05), and this area exhibited the strongest warming trend in China over the past 15 years. Rapid warming has a significant impact on the local area. The Northwest Region (V) is an arid and semiarid area dominated by temperate and warm temperate climates. This region features plateaus, basins and deserts. Due to the lack of precipitation, the main water resource in the northwest is alpine ice and snowmelt, which is more susceptible to temperature changes. In the large-scale water-deficient areas in the Northwest Region, the impacts of climate warming on local water resources and the ecological environment are more significant than in other areas. On the one hand, increasing the frequency and intensity of drought causes the degradation of fragile local vegetation, the shrinkage of oasis areas, and an increase in the vulnerability of the ecological environment. On the other hand, high temperatures will release more alpine meltwater, increasing surface runoff, and greatly alleviating local water stress, although this is less helpful for areas with few ice reserves. However, the rapid degradation of glaciers as a result of rapid and sustained warming may bring more potential threats to the ecological environmental balance and biological survival. Finally, due to the sparse vegetation

https://doi.org/10.5194/essd-2019-155
Preprint. Discussion started: 11 October 2019

in the Northwest Region (V), it is necessary to carry out and increase ecological engineering, such as the Three-North Shelterbelt Program. Furthermore, increased vegetation cover is conducive to increasing the soil water content, improving local land desertification and ever-expanding soil erosion. In addition, in terms of vegetation, the local regulation of greenhouse gases and evapotranspiration can be used to generate positive feedback on the stability of the surface temperature.

In the Qinghai-Tibet Plateau Region (VI), the ecological environment is complex, and the unique plateau terrain and thermal properties of the surrounding areas play an important role in regulating the surrounding atmospheric circulation system. Because the Qinghai-Tibet Plateau is extremely sensitive to climate change, it is considered to be a key area of global climate change. Therefore, we have also paid close attention to the temperature changes on the Tibetan Plateau. As shown in Fig. 6a and b, an obvious positive trend was captured in the southern part of the Qinghai-Tibet region (slope>0.08), which should be emphasized. Meanwhile, the warming trend in the Qaidam Basin in the northeast is significantly higher (slope > 0.1) than that in the surrounding area. This result may be associated with the complex geological structure of the Qaidam Basin. There are many fault structures in the Qaidam Basin. When subjected to geostress, the rock movement increases, and the compression displacement between the rock layers releases energy during the process of mechanical friction. This process also provides good geothermal conductivity to the upper strata. The geological conditions lead to an abnormal increase in surface temperature. The Tanggula Mountains in the central part of the Qinghai-Tibet Plateau and the southern Tibetan Valley in the south exhibit a significant warming trend, while the northern part does not exhibit significant changes. This result may be due to the different effects of the monsoon circulation: Qinghai Province in the northern part of the Tanggula Mountain is mainly controlled by the East Asian monsoon, while the southern part of the southern Tibet Valley is affected by the South Asian monsoon.

4.1.2 Day and night change analysis

To more specifically assess the interannual changes in LST, we further analyzed the diurnal trends in LST. The spatial distribution of the average annual diurnal surface temperature in the time series is shown in Fig. 7. During the day, the warming trend mainly comes from the eastern part of North China, the central and western parts of the northwest, and the southern part of the Qinghai-Tibet Plateau. The annual daytime warming/cooling trends of surface temperature in almost all regions from 2003 to 2017 are significantly higher than those in the evening (-0.03<slope<0.03); thus, the average LST warming/cooling trends can be attributed to the changes during the daytime. The diurnal variation in LST also indicates that the trend of LST changes is more likely due to factors such as daytime human activities and sunshine hours. The effects of changes in solar radiation on the near-surface thermal conditions are the most pronounced. Among these changes, the warming trend in the southern part of the Qinghai-Tibet Plateau is obvious (slope>0.09). Duan and Xiao (2015) found that since 1998, the amount of daytime cloud cover in the southern part of the Qinghai-Tibet Plateau has decreased rapidly, resulting in an increase in sunshine hours. The increase in solar radiation during the day will directly lead to an increase in surface temperature, which is an important factor leading to an increase in daytime temperature. However, compared with the daytime, the interannual temperature change trend at night is relatively gentle and can be considered stable.

https://doi.org/10.5194/essd-2019-155
Preprint. Discussion started: 11 October 2019

Insert Figure 7 here

Figure 7: Spatial dynamics of interannual diurnal LST change trends from slope (a) and correlation coefficient (b).

485 **4.1.3 Analysis of the diurnal temperature difference**

Figure. 8 shows the spatial distribution of the average daytime LST, average nighttime LST, and day and night temperature differences. The LST shows significant spatial variation. During the day, the distribution of LST varies with surface insolation depending on the solar zenith angle (Jin and Liang, 2006). The highest LST during the day appears in the northwestern part of V and the desert area of the Tarim Basin in the Alashan Plateau (30 °C to more than 35 °C), rather than 490 in the southern part of the low-latitude tropics, which is different from the patterns at night. Except for the Qinghai-Tibet Plateau, the nighttime LST decreases from the southern low-latitude areas to the northern high latitude areas, and the spatial variation is roughly consistent throughout the six subregions. This result also suggests that the temperature change is significantly related to the latitudinal range.

As shown in Fig. 8c, the largest diurnal difference in LST is concentrated mainly in the mountainous area of the Qinghai-495 Tibet Plateau; this difference is greater than 25 °C and is especially prominent in the Qaidam Basin. The lowest diurnal LST difference of less than 5 °C can be seen at low latitudes along the southeastern coast in South China. At the same time, affected by the height of the plateau, the temperature difference between day and night in the Yunnan-Guizhou Plateau in the western part of Central China is 11-15 °C, while that in the eastern area at the same latitude is only 6-11 °C. At the same time, compared with the inland areas at similar latitudes, the coastal areas (II and III in the eastern part of Central China and 500 the central and eastern parts of the South China Region) usually have small diurnal LST differences.

As shown in Fig. 8c, the average annual diurnal LST difference from 2003 to 2017 is characterized by the blue line AB, which indicates the boundary between the eastern China and western China. The blue line AB in the picture is the Hu Line, which was proposed by Hu Huanyong in 1938. The Hu Line is the connecting line between Heihe County in Heilongjiang Province in northern China and Tengchong in Yunnan Province. The Hu Line is not only the transition line for China's 505 ecological environment but also the dividing line for China's population density. The east side of the Hu Line is dominated by geographical structures such as plains and hills, and its economy is developed. The east side is a densely populated area, accounting for 94 % of China's population. The west side is dominated by plateaus, mountains and basins. The western part is vast but accounts for only 6 % of China's population. Development is slow in this area. The temperature difference between day and night on the eastern side of the Hu Line is generally small (average at 11.8 °C), and the temperature 510 difference between day and night on the western side is large (average at 21.9 °C). This distribution of day and night temperature differences is an interesting phenomenon.

Insert Figure 8 here

Figure 8. Spatial dynamics of average daytime LST(a), average nighttime LST (b)and difference between daytime and nighttime (c)from 2003 to 2017

https://doi.org/10.5194/essd-2019-155
Preprint. Discussion started: 11 October 2019

515 **4.2 Seasonal change analysis**

In addition to analyzing the characteristics of the interannual variation in LST, we also conducted an analysis of the seasonal variation characteristics to further reveal the LST variation patterns in detail (see Fig. 9). The variation characteristics are also described by the slope of the change and the correlation coefficient (R) proposed in Section 3.4.1. The results show that there is a significant spatial difference between the seasonal surface temperature trends, reflecting the effect of seasonal
520 temperature changes on regional temperature changes. From 2003 to 2017, the trend of warming in the four seasons was most significant in winter, which exhibited the largest warming area (accounting for 70 %), followed by that in spring and summer, and the national average LST change in autumn basically did not change. Compared with the global warming hiatus that occurred from 1998 to 2002, the warming trends in China showed large differences in the four seasons (Li et al., 2015).

Specifically, in spring, the warming area is concentrated in the northern areas (I, II, V), while the southern areas
525 experienced a weak cooling trend. In the northern areas, the Northwest Region (V) and the Northeast Region (I) show dramatic warming trends where the slope is greater than 0.06 (see Fig. 9a2), with the Inner Mongolia Plateau and the northwestern part of the Greater Khingan Range exhibiting the most prominent warming trends. In addition, rapid warming also occurred in the North China Plain in the eastern part of the North China Region (II) (especially near Beijing and some areas of Hebei Province, slope=0.12, R=0.57, P<0.05), which may be unfavorable for crop growth in the North China Plain,
530 especially for winter wheat. This impact occurs because the increase in temperature is an important factor in increasing the frequency and intensity of drought, which will greatly reduce the crop yield (He et al., 2016; Ayantobo et al., 2017). In the Northeast Region (I), spring exhibited the greatest warming, while a negative trend was detected in other seasons.

As shown in Fig. 9, both summer and autumn showed nonsignificant warming trends throughout the country. In summer, there were slightly increasing trends almost everywhere in China, while negative trends were still observed in the Northeast
535 Region (I) (details in Fig. 9). The slight warming trends might occur due to the weakening of the East Asian summer monsoon circulation caused by the tropical high-altitude composition of the easterly jet (TEJ) (Ding Y et al., 2008). The Chinese atmospheric circulation system is significantly affected by the East Asian summer monsoon. The location of the monsoon movement and the pattern of changes in monsoon velocity and intensity affect the change in surface temperature. At the same time, summer precipitation in the northwestern region has increased in recent years, which may have helped
540 slow the rapid warming in the region (He et al., 2016). In autumn, the cooling trends mainly come from the Northeast Region (I) and the Northern Chinese Tianshan Mountains in the Qinghai-Tibet Plateau Region (VI). The Qinghai-Tibet Plateau was still controlled by the strong warming trends (near Lhasa city, slope=0.09, R=0.60, P<0.05), especially in the southern part of the Tanggula Mountains.

In winter, 69.4 % of the areas are warming, which is significantly higher than that in other seasons; thus, winter is the
545 most important source of interannual increases in the average LST. The most remarkable warming trend comes from the Northwest Region (V) and the Qinghai-Tibet Plateau Region (VI) in winter. In particular, these large-scale rapid warming patterns that occurred in winter are worthy of attention. This warming might occur due to excessive emissions of

https://doi.org/10.5194/essd-2019-155
Preprint. Discussion started: 11 October 2019

atmospheric greenhouse gases and black carbon aerosols caused by human activities, which are most pronounced in winter (Hu, 2003; Stine et al., 2009). The LST in the central and western parts of the Northwest Region (V) increased significantly (in most areas, slope >0.080, R>0.71, P<0.05). This result might be attributed to the weakening of the Siberian high-pressure system in the region. The Siberian high-pressure system originates from the powerful high-pressure system in the cold Mongolian-Siberian region, which drives a large number of cold and dry air masses to move south to promote rapid cooling in the eastern part of Asia. Li et al. (2012) calculated the correlation between winter temperatures and the Siberian high-pressure index: R = 0.715, P < 0.001, indicating that winter temperatures in northwestern China are significantly correlated with the Siberian high-pressure index. In addition, a large number of significant warming areas formed on both sides of the western Tianshan Mountains, which are oases. We believe that warming may be related to the increase in greenhouse gases generated by human activities during the expansion of urbanization.

Insert Figure 9 here

Figure 9: The interseasonal variability rates (slope) and correlation coefficients (R) of LST in spring (a), summer (b), autumn (c) and winter (d) from 2003 to 2017, a1, b1, c1 and d1 are the spatial distributions of the slopes at the four seasons, a2, b2, c2 and d2 are histograms of the slope of the four seasons, and a3, b3, c3 and d3 are the spatial distribution of the correlation coefficient (R) at the four seasons.

4.3 Monthly average change analysis

We further analyze the interannual variation in the LST for each month in the time series. As shown in Fig. 10, in the past 15 years, the monthly average change in the LST was more significant than the seasonal and annual changes. Eight months showed warming trends (slope>0), which is obviously more than the number of months that showed cooling trends. The warming trends in the second half of the year (mainly concentrated in July, August, October, December) were significantly higher than those in the first half of the year. The largest warming trends were observed in July (slope=0.063), and 76 % of the areas showed warming trends. Relatively significant warming ($slope_{mean}$>0.04) occurred in the Northwest Region (V), North China Region (II) and Qinghai-Tibet Plateau Region (VI). December also showed a relatively higher warming trend, accounting for 72 % of the area, and the significantly warmed areas were concentrated in the northwest and Qinghai Tibetan areas. However, no significant cooling trend (slope <0.05) occurred in the 12-month period. The widest cooling trend was found in the Northeast Region and South China. In the Northeast Region, the cooling trend was captured in February and October, while in South China, January and April contributed the most to cooling.

Insert Figure 10 here

Figure 10: The monthly variability rates from slope (a) and correlation coefficients (b) of LST from 2003 to 2017.

https://doi.org/10.5194/essd-2019-155
Preprint. Discussion started: 11 October 2019

5 Verification and discussion

MODIS exhibits good performance in retrieving LST data, which has been verified by various studies (Wan et al., 2004, Wan, 2008, Wan and Li, 2011, Wan, 2014). Furthermore, to better evaluate the accuracy of the new dataset, we performed verification for different regions using independent in situ data (subset (2) in Section 3.2) that was not used during the reconstruction process. Fig. 11 shows the statistical results of the difference between the two types of data in six natural subregions (shown in blue in the scatterplot). Three statistical accuracy measures are used to evaluate the accuracy of the calibration: the square root of the Pearson coefficient (R^2), root mean squared error (RMSE) and mean absolute error (MAE). All subregions showed good agreements between MODIS LST and meteorological station data. The R^2 values varied from 0.93 to 0.99, with an average of 0.97. The RMSE ranged from 1.24 °C to 1.58 °C, with an average of 1.39 °C. A relatively large RMSE between the reconstructed LST and ground-based LST appeared in some sites in the Qinghai-Tibet Plateau Region, indicating that the temperature exhibited great spatial heterogeneity over the complex terrain. The MAE varied from 1.23 °C to 1.37 °C, with an average of 1.30 °C. These results indicate that the reconstructed MODIS LST dataset is robust and accurate due to its high consistency with the in situ data. Therefore, we believe that the accuracy of LST data can be improved by this method.

Insert Figure 11 here

Figure 11: The scatter diagrams in six natural subregions (I, II, III, IV, V, VI) between the ground station data and the MODIS LST data. The blue scatter indicates the verification result of the reconstructed MODIS LST, and its statistical accuracy measures (R^2, RMSE, MAE) are also indicated. The result of the linear model corrected corrected is indicated in gray.

To further understand the credibility of the data and clarify the limitations of the use of this method, we further assess the performance in terms of the seasonal bias and compared it with the original seasonal LST data. Verification ground stations collected in representative areas are selected to help illustrate the distribution of the error in the reconstructed data (six key zones are identified, corresponding to the a, b, c, d, e, and f areas shown by the red circles in Fig. 1, an overview of the ground stations can be found in Table 1. The six key zones are selected, including the three most significant regions for warming (b, d, f), the two most significant regions for cooling (a, c) and the zone located in Xinjiang Province (see Fig. 6a for details). Two of the zones, zone (a) located in the Northeast Region and zone (b) located in the North China Region, experienced the strongest cooling trend and significant warming, respectively. Simultaneously, these two regions are important food-producing areas in China. The rapid changes in LST have a major impact on the stability of crop yields and the adjustment of crop planting systems. In addition, the Qinghai-Tibet Plateau, where key zone f is located, has a unique climate and is highly sensitive to climate change, which is of great significance for maintaining the ecological security of Asia (Xu et al., 2008). In particular, special attention was given to the Sahara Desert region (e) in Xinjiang, which has complex terrain and extensive heterogeneity.

https://doi.org/10.5194/essd-2019-155
Preprint. Discussion started: 11 October 2019

Seasonal scale verification was evaluated using MODIS data (including the original LST and reconstructed LST) and ground-based LST RMSE for comparison in six key zones, as shown in Table 2. Compared with the original LST, the average RMSE decreased by 18 % from 1.79 °C to 1.46 °C. Both datasets exhibited the largest RMSE in summer and the smallest in autumn, indicating that the original and reconstructed LST data have highly consistent seasonal patterns. For the reconstructed LST data, we further found that the RMSE values at some sites in the summer were significantly higher than those at other sites. The regions that exhibited high RMSE values were mainly concentrated in the western regions (Xinjiang, Inner Mongolia and the Qinghai-Tibet Plateau), while the values in the other three regions were relatively small. The main reason for this difference may be the complex and diverse terrain and large climate differences in the western region. The average RMSE in autumn was the smallest at 1.07 °C. The winter RMSE ranged from 0.04 to 3.81, with an average of 1.45 °C.

For the reconstructed LST data, the distribution of the RMSE varied greatly between the eastern and western regions at the seasonal scale. The maximum RMSE values for all stations in the eastern typical zones (i.e., key zone a in the Northeast Region (I), key zone b in the North China Region (II)) occurred in the cold winter, while the highest values for most sites in the western region occurred during the hot summer months (i.e., the remaining four zones). At the same time, the comparison results show that the mean RMSE between the ground-based observation data and the LST data was significantly higher in the western region than in the eastern region (mean 1.04 °C in eastern regions I and II and 1.69 °C in western regions IV, V, and VI). The large spatial variations in temperature caused by the complex terrain in the western region may be the cause of large errors. At the same time, a large RMSE between the reconstructed LST and the ground-based LST appeared in some locations in Inner Mongolia (i.e., key zone e) in the Northwest Region, further indicating that the temperature over complex terrain exhibited great spatial heterogeneity.

We also note that the selected ground stations shown in Table 2 located in six key zones are examples where the local LST warming/cooling rate changed by more than the general rate, so the theoretical error rate is higher than that in other regions. Moreover, the examples indicate that the reconstruction model proposed here is effective even in the areas most likely to exhibit errors. As the temperature changes more smoothly and more in line with the trend of the general temperature changes, the accuracy will increase.

According to the scatterplots of the ground station data and the reconstructed MODIS LST data shown in blue in Fig. 11, here we employed a correction model that uses the results of linear regression analysis between the two data to further improve the accuracy. The goal of the calibration model reduces or eliminates the combined error introduced by various variables, so six subregions with different climatic conditions are corrected separately to obtain better calibration results for the study area. At the same time, in order to eliminate the difference of the six regions edge boundary areas, smooth constraints are imposed on some of edge pixels with significant differences to guarantee the consistency of the regions. The comparisons of the corrected LST data with the ground station data are indicated by the gray points in Fig. 11. In this study, the main reason for adopting the regression analysis model is the reality that the robust reconstruction results have obtained through a large amount of work for which a linear model can further improve the results. The results show that the results of

https://doi.org/10.5194/essd-2019-155
Preprint. Discussion started: 11 October 2019

model reconstruction are more consistent with the ground station data, which effectively improves the problem of underestimation of MODIS LST data in some areas.

Table 2. RMSEs of seasonal LST between monthly LST (including the original LST and reconstructed LST) and ground-based LST (Orig. indicates the original LST located at ground stations. Recon. indicates the reconstructed LST located at ground stations)

Insert Table 2 here

The verification results show that the dataset has reasonable consistency with the in situ measurements, indicating that the interference of cloud coverage is well eliminated. The dataset obtained after reconstruction is a large-scale, long-term, unique surface temperature dataset because it eliminates low-quality pixels caused by factors such as cloud disturbance and achieves complete coverage of the entire study region. The accuracy and spatiotemporal continuity of this dataset are greatly improved compared to those of the original MODIS monthly data. Moreover, in this dataset, the true ground surface temperatures under cloud coverage are retrieved instead of reconstructing the LST under clear-sky conditions, which is better than the methods used in many previous studies.

At the same time, the reconstruction strategy that combines monthly data with daily data effectively solves the problem of reconstructing real LST data under cloud coverage with very limited information and improves the accuracy of the monthly data reconstruction results. The final linear correction model improves the consistency of the LST data with terrestrial data. We believe that these datasets can be applied to research regional agricultural ecological environments and to monitor agrometeorological disasters. In a small range of practical applications, such as urban heat island monitoring, our current data may not be suitable for monitoring in great detail due to the coarse resolution, which is something we need to improve in future work.

6 Data availability

The LST dataset in China is distributed under a Creative Commons Attribution 4.0 License. The data is freely available in the Zenodo repository https://doi.org/10.5281/zenodo.3378912 (Zhao et al., 2019).Vector files for six natural subregions can also be obtained from the same link.

7 Summary and conclusions

Based on the Terra and Aqua MODIS land surface temperature dataset and meteorological station data, a new LST dataset over China was established for the period from 2003-2017. This dataset effectively removed approximately 20 % of the missing pixels or poor-quality LST pixels contaminated by clouds in the original MODIS monthly image. A detailed comparison and analysis with the in situ measurements shows that the reconstruction results has high precision, the average RMSE is 1.39 °C, the MAE is 1.30 °C and R^2 is 0.97. The data are freely available at

https://doi.org/10.5194/essd-2019-155
Preprint. Discussion started: 11 October 2019

https://doi.org/10.5281/zenodo.3378912 (Zhao et al., 2019). We believe that this dataset will be of great use in research related to temperature, such as high temperature and drought studies, because it effectively overcomes the limitations of reconstructing the real LST under cloudy conditions in the past and achieves good spatiotemporal coverage.

The constructed high-precision monthly LST dataset for China provides a detailed perspective of the patterns of the spatial and temporal changes in LST. The LST dataset was used to analyze the regional characteristics and capture the variations in LST at the annual, seasonal and monthly scales. Our results showed that the LST showed a slight upward trend with a slope of 0.011 (approximately 63.7 % and 20.80 % of the pixels underwent warming and significant warming, respectively). There were great regional differences in the climate warming trend. In the Northwest Region, the Qinghai-Tibet Plateau Region and the North China Plain experienced significant warming trends (i.e., the slope ranged from 0.025 to greater than 0.1). The impacts of human activities on warming, such as the increase in greenhouse gases and black carbon aerosol emissions from urbanization and industrial and agricultural development, are prominent. Greenhouse gases absorb infrared longwave radiation from the ground, which results in a positive feedback effect on warming. Moreover, the coupling of greenhouse gases and monsoons will result in changes in the energy budget in the monsoon region, which will affect the intensity of monsoon circulation. At the same time, the change in temperature in the short term may be affected by the increase in aerosols such as PM2.5 and black carbon emitted from atmospheric pollutants. Carbon aerosol pollution will heat the flow of air and reduce the cooling effect of solar radiation reaching the surface, affecting local or even global climate changes. Especially in rapidly expanding urban areas, such as North China and the Yangtze River Delta, the impact of human activities on temperature trends will be more pronounced.

Meanwhile, a cooling trend was also observed in China: most areas of the Northeast Region became markedly colder, especially in the Songnen Plains in the middle of the region (i.e., slope=-0.11, $R=0.61$, $P<0.05$). South China also showed a slight cooling trend. The interannual temperature changes indicated that the daytime temperature changed more intensely than the nighttime temperature, which may be closely related to changes in solar radiation and the release of large amounts of greenhouse gases from human activities. Earth rotation is the factor that determines seasonal change, which is also affected by monsoon changes, ocean currents and other factors. The LST trends showed significant changes in the different seasons. The warming trend in winter was the most significant compared with that in the other three seasons, especially in the northwestern region of the arid and semiarid zone and the Qinghai-Tibet Plateau. As a key parameter for different research fields, such as simulating land surface energy and water balance systems, LST provides important information for monitoring and understanding high temperature and drought conditions, which must be taken into consideration for agricultural production and meteorological research. Therefore, we believe that the LST dataset produced in this study can be useful for drought research and monitoring and can be further used for agricultural production and climate change research.

Author contributions. KM and YC designed the research and developed the methodology, BZ and XM supervised the downloading and processing of satellite images, BZ wrote the manuscript, and JS, ZL and ZQ and all authors revised the manuscript.

Competing interests. The authors declare no conflicts of interest.

Acknowledgments. This research was funded by the National Key R&D Program Key Project (Global Meteorological Satellite Remote Sensing Dynamic Monitoring, Analysis Technology and Quantitative Application Method and Platform Research (2018YFC1506502) & Multi-source meteorological data fusion technology research and product development (2018YFC1506602)), National Natural Science Foundation of China (41571427) and Open Fund of State Key Laboratory of Remote Sensing Science (Grant No. OFSLRSS201910). The authors would also like to thank the National Aeronautics and Space Administration (NASA) for their support in LST product and elevation data. We also thank the China Meteorological Administration for providing the Meteorological LST data.

References

André, C., Ottlé, C., Royer, A., and Maignan, F.: Land surface temperature retrieval over circumpolar arctic using ssm/i–ssmis and modis data. Remote Sens. Environ., 162, 1–10, https://doi.org/10.1016/j.rse.2015.01.028, 2015.

Ayantobo, O. O., Li, Y., Song, S., and Yao, N.: Spatial comparability of drought characteristics and related return periods in mainland china over 1961-2013. J Hydrol., 550, 549-567, https://doi.org/10.1016/j.jhydrol.2017.05.019, 2017.

Benali, A., Carvalho, A. C., Nunes, J. P., Carvalhais, N., and Santos, A.: Estimating air surface temperature in Portugal using MODIS LST data. Remote Sens. Environ., 124, 108-121, https://doi.org/10.1016/j.rse.2012.04.024, 2012.

Crosson, W. L., Al-Hamdan, M. Z., Hemmings, S. N. J., and Wade, G. M.: A daily merged MODIS Aqua–Terra land surface temperature dataset for the conterminous United States. Remote Sens. Environ., 119, 315–324, https://doi.org/10.1016/j.rse.2011.12.019, 2012.

Deng, M. J.: "Three Water Lines" strategy: Its spatial patterns and effects on water resources allocation in northwest China. J Geogr., 73, 1189-1203, https://doi.org/10.11821/dlxb201807001, 2018 (in Chinese).

Ding, Y., Wang, Z., and Sun, Y.: Inter‐decadal variation of the summer precipitation in East China and its association with decreasing Asian summer monsoon. Part I: Observed evidences. Int J Climatol., 28, 1139–1161, https://doi.org/10.1002/joc.1615, 2008.

Duan, A. and Xiao, Z.: Does the climate warming hiatus exist over the Tibetan Plateau? Sci Rep., 5, 13711, https://doi.org/10.1038/srep13711, 2015.

Fan, X., Liu, H., Liu, G., and Li, S.: Reconstruction of modis land-surface temperature in a flat terrain and fragmented landscape. Int. J. Remote Sens., 35, 7857–7877, https://doi.org/10.1080/01431161.2014.978036, 2014.

https://doi.org/10.5194/essd-2019-155
Preprint. Discussion started: 11 October 2019

Gafurov, A. and Bárdossy, A.: Cloud removal methodology from MODIS snow cover product, Hydrol. Earth Syst. Sci. Data., 13, 1361–1373, https://doi.org/10.5194/hess-13-1361-2009, 2009.

Gao, L., Wei, J., Wang, L., Bernhardt, M., and Schulz, K.: A high-resolution air temperature dataset for the Chinese Tian Shan in 1979–2016. Earth Syst. Sci. Data., 10, 2097-2114, https://doi.org/10.5194/essd-10-2097-2018, 2018.

Hansen, J., Ruedy, R., Sato, M., and Lo, K.: Global surface temperature change. Rev Geophys., 48, RG4004, https://doi.org/10.1029/2010RG000345, 2010.

He, J., Yang, X., Li, Z., Zhang, X., and Tang, Q.: Spatiotemporal Variations of Meteorological Droughts in China During 1961–2014: An Investigation Based on Multi-Threshold Identification. Int J Disast Risk Sc., 7, 63-76, https://doi.org/10.1007/s13753-016-0083-8, 2016.

Hu, Z. Z.: Long-term climate variations in China and global warming signals. J Geophys Res., 108, 4614, https://doi.org/10.1029/2003JD003651, 2003.

Jin, M. and Liang, S. L.: An improving land surface emissively parameter of land surface models using global Remote Sens observations J. Clim., 19, 2867–81, https://doi.org/10.1175/jcli3720.1, 2006.

Jin, M. L. and Dickinson, R. E.: Land surface skin temperature climatology: benefitting from the strengths of satellite observations. Environ. Res. Lett., 5, 044004, https://doi.org/10.1088/1748-9326/5/4/044004, 2010.

Ke, L., Ding, X., and Song, C.: Reconstruction of Time-Series MODIS LST in Central Qinghai-Tibet Plateau Using Geostatistical Approach. IEEE Geosci. Remote Sens Lett., 10, 1602-1606, https://doi.org/10.1109/LGRS.2013.2263553, 2013.

Li, B., Chen, Y., and Shi, X.: Why does the temperature rise faster in the arid region of northwest China? J Geophys Res-Atmos., 117, 1-7, https://doi.org/10.1029/2012JD017953, 2012.

Li, Q., Yang, S., Xu, W., Wang, X. L., Jones, P., Parker, D., Zhou, L. M., Feng, Y., and Gao, Y.: China experiencing the recent warming hiatus. Geophys Res Lett., 42, 889-898, https://doi.org/ 10.1002/2014GL062773, 2015.

Liu, H., Li, X., Fischer, G., and Sun, L.: Study on the Impacts of Climate Change on China's Agriculture. Climatic Change., 65, 125-148, https://doi.org/125–148,10.1023/B:CLIM.0000037490.17099.97, 2004.

Li, Z. L., Wu, H., Wang, N., Qiu, S., Sobrino, J.A., Wan, Z., Tang, B. H., and Yan, G.: Land surface emissivity retrieval from satellite data. Int. J. Remote Sens., 34, 3084–3127, https://doi.org/10.1080/01431161.2012.716540,2013.

Ma, X. L., Wan, Z., Moeller, C. C., Menzel, W. P., Gumley, L. E., and Zhang, Y.: Retrieval of geophysical parameters from Moderate Resolution Imaging Spectroradiometer thermal infrared data: evaluation of a twostep physical algorithm. Applied Optics., 39, 3537 – 3550, https://doi.org/10.1364/AO.39.003537, 2000.

Ma, X. L., Wan, Z., Moeller, C. C., Menzel, W. P., and Gumley, L. E.: Simultaneous retrieval of atmospheric profiles and land-surface temperature, and surface emissivity from Moderate Resolution Imaging Spectroradiometer thermal infrared data: extension of a two-step physical algorithm. Applied Optics., 41, 909 – 924, https://doi.org/10.1364/AO.41.000909,2002.

https://doi.org/10.5194/essd-2019-155
Preprint. Discussion started: 11 October 2019

Mao, K. B., Shi, J. C., Li, Z. L., Qin, Z. H., Li, M. C., and Xu, B.: A physics-based statistical algorithm for retrieving land surface temperature from AMSR-E passive microwave data,Sci China Ser D-Earth Sci., 50, 1115-1120, https://doi.org/10.1007/s11430-007-2053-x, 2007.

Mao, K. B., Zuo, Z.Y., Shen, X. Y., Xu, T. R., Gao, C.Y., and Liu,G.: Retrieval of Land-surface Temperature from AMSR2 Data Using a Deep Dynamic Learning Neural Network, Chinese Geogr Sci., 28, 1-11, https://doi.org/1–11,10.1007/s11769-018-0930-1, 2018.

Mao, K. B., Yuan, Z.J., Zuo, Z.Y., Xu, T. R., Shen, X. Y., and Gao, C.Y.: Changes in Global Cloud Cover Based on Remote Sens Data from 2003 to 2012, Chinese Geogr Sci., 29, 306–315, https://doi.org/CNKI:SUN:ZDKX.0.2019-02-011, 2019.

Markus, M., Duccio, R and Markus, N.: Surface Temperatures at the Continental Scale: Tracking Changes with Remote Sensing at Unprecedented Detail. Remote Sens., 2, 333-351, https://doi.org/10.3390/rs6053822,2010.

McMillin, L. M.: Estimation of sea surface temperature from two infrared pixel window measurements with different absorptions. J. Geophys. Res., 80, 5113–5117, 1975.

Na, F., Gaodi, X., Wenhua, L., Yajing, Z., Changshun, Z., and Na, L.: Mapping air temperature in the lancang river basin using the reconstructed modis LST data. J. Res. Ecol., 5, 253–262, https://doi.org/10.5814/j.issn.1674-764x.2014.03.008, 2014.

Neteler, M.: Estimating daily land surface temperatures in mountainous environments by reconstructed MODIS LST data, Remote Sens., 2, 333–351,https://doi.org/10.3390/rs1020333, 2010.

Oku, Y., H. Ishikawa, S. Haginoya., and Y. Ma. : Recent trends in land surface temperature on the Tibetan Plateau, J. Clim., 15, 2995– 3003,https://doi.org/10.1175/JCLI3811.1, 2006.

Prigent, C., Jimenez, C., and Aires, F.: Toward “all weather” long record, and real-time land surface temperature retrievals from microwave satellite observations. J. Geophys. Res. Atmos., 121, 5699–5717. 24, 2016.

Scharlemann, J.P., Benz, D., Hay, S.I., Purse, B.V., Tatem, A.J., Wint, G.R., and Rogers, D.J.: Global data for ecology and epidemiology: A novel algorithm for temporal Fourier processing MODIS data. PLoS One., 3: e1408-10.1371, https://doi.org/10.1371/journal.pone.0001408, 2008.

Stine, A. R., Huybers, P., and Fung, I. Y.: Changes in the phase of the annual cycle of surface temperature, Nature., 457, 435–440, https://doi.org/ 10.1038/nature07675, 2009.

Stocker, T.F., Qin, D., Plattner, G.-K., Tignor, M., Allen, S.K., Boschung, J., Nauels, A., Xia, Y., Bex, V, and Midgley, P.M. (Eds.): IPCC, 2013: Climate Change 2013: The Physical Science Basis. Contribution of Working Group I to the Fifth Assessment Report of the Intergovernmental Panel on Climate Change. Cambridge University Press, Cambridge, United Kingdom and New York, NY, USA, 2013.

Sun, L., Chen, Z., Gao, F., Anderson, M., Song, L., Wang, L., Hu, B., and Yang, Y.: Reconstructing daily clear-sky land surface temperature for cloudy regions from modis data. Comput. Geosci., 105, 10–20, https://doi.org/10.1016/j.cageo.2017.04.007, 2017.

https://doi.org/10.5194/essd-2019-155
Preprint. Discussion started: 11 October 2019

Tatem, A.J., Goetz, S.J., and Hay, S.I.: Terra and Aqua: new data for epidemiology and public health. Int. J. Appl. Earth Obs. Geoinf., 6, 33-46, https://doi.org/10.1016/j.jag.2004.07.001, 2004.

Vancutsem, C., Ceccato, P., Dinku, T., and Connor, S. J.: Evaluation of MODIS land surface temperature data to estimate air temperature in different ecosystems over Africa. Remote Sens. Environ., 114, 449–465, https://doi.org/10.1016/j.rse.2009.10.002, 2010.

Wan, Z. M.: Collection-5 MODIS Land Surface Temperature Products Users' Guide [EB/OL], 2007.

Wan, Z. M.: New refinements and validation of the MODIS landsurface temperature/emissivity products. Remote Sens. Environ., 112, 59–74 https://doi.org/ 10.1016/j.rse.2006.06.026, 2008.

Wan, Z. M.: New refinements and validation of the collection-6 MODIS land-surface temperature/emissivity product. Remote Sens. Environ., 140, 36–45, https://doi.org/10.1016/j.rse.2013.08.027,2014.

Wan, Z. M. and Dozier, J.: A generalized split-window algorithm for retrieving land-surface temperature from space. IEEE T Geosci Remote., 34, 892–905, https://doi.org/ 10.1109/36.508406, 1996.

Wan, Z. M. and Li, Z. L.: A physics-based algorithm for retrieving landsurface emissivity and temperature from EOS/MODIS data. IEEE T Geosci Remote., 35, 980– 996, https://doi.org/10.1109/36.602541, 1997.

Wan, Z. M. and Li, Z. L.: MODIS land surface temperature and emissivity. Remote Sens. and Digital Image Proc., 11, 563-577, https://doi.org/ 10.1007/978-1-4419-6749-7_25, 2011.

Wan, Z. M., Zhang, Y., Zhang, Q., and Li, Z. l.: Validation of the land-surface temperature products retrieved from Terra Moderate Resolution Imaging Spectroradiometer data. Remote Sens. Environ., 83, 163–180, https://doi.org/10.1016/j.rse.2009.10.002, 2002.

Wan, Z. M., Zhang Y, Zhang Q., and Li Z L.: Quality assessment and validation of the MODIS global land surface temperature. Int J Remote Sen S., 25, 261–274 https://doi.org/ 10.1080/0143116031000116417, 2004.

Wang, K. and S. Liang.: Evaluation of ASTER and MODIS land surface temperature and emissivity products using long-term surface longwave radiation observations at SURFRAD sites, Remote Sens. Environ., 113, 1556–1565, https://doi.org/10.1016/j.rse.2009.03.009, 2009.

Wang, K., Wan, Z., Wang, P., Sparrow, M., Liu, J., and Haginoya, S.: Evaluation and improvement of the MODIS land surface temperature/emissivity products using ground-based measurements at a semi-desert site on the western Tibetan Plateau, Int. J. Remote Sens., 28, 2549–2565, https://doi.org/10.1080/01431160600702665, 2007.

Xu, Y. and Shen, Y.: Reconstruction of the land surface temperature time series using harmonic analysis. Comput. Geosci., 61, 126–132, https://doi.org/10.1016/j.cageo.2013.08.009, 2013.

Xu, X., Lu, C., Shi, X., and Gao, S.: World water tower: an atmospheric perspective. Geophysical Research Letters., 35, L20815, https://doi.org/10.1029/2008GL035867, 2008.

Yang, X., Lin, E., Ma, S. M., Ju, H., Guo, L. P., Xiong., Li, Y., and Xu, Y. L.: Adaptation of agriculture to warming in Northeast China. Climatic Change., 84, 45-58, https://doi.org/10.1007/s10584-007-9265-0, 2007.

https://doi.org/10.5194/essd-2019-155
Preprint. Discussion started: 11 October 2019

Yu, W. J., Nan, Z. T., Wang, Z. W., Chen, H., Wu, T. H., and Zhao, L.: An Effective Interpolation Method for MODIS Land Surface Temperature on the Qinghai–Tibet Plateau. IEEE J. Sel. Topics Appl. Earth Observ. Remote Sens., 8, 4539-4550, https://doi.org/10.1109/JSTARS.2015.2464094, 2015.

Zeng, C., Shen, H., and Zhang, L.: Recovering missing pixels for Landsat ETM+ SLC-off imagery using multitemporal regression analysis and a regularization method, Remote Sens. Environ., 131, 182–194, https://doi.org/10.1016/j.rse.2012.12.012, 2013.

Zhao, B., Mao, K. B., Cai, Y. L., Shi, J. C., Li, Z. L., Qin, Z. H., and Meng, X. J.: A combined Terra and Aqua MODIS land surface temperature and meteorological station data product for China from 2003–2017 [Dataset], Zenodo, https://doi.org/10.5281/zenodo.3378912, 2019.

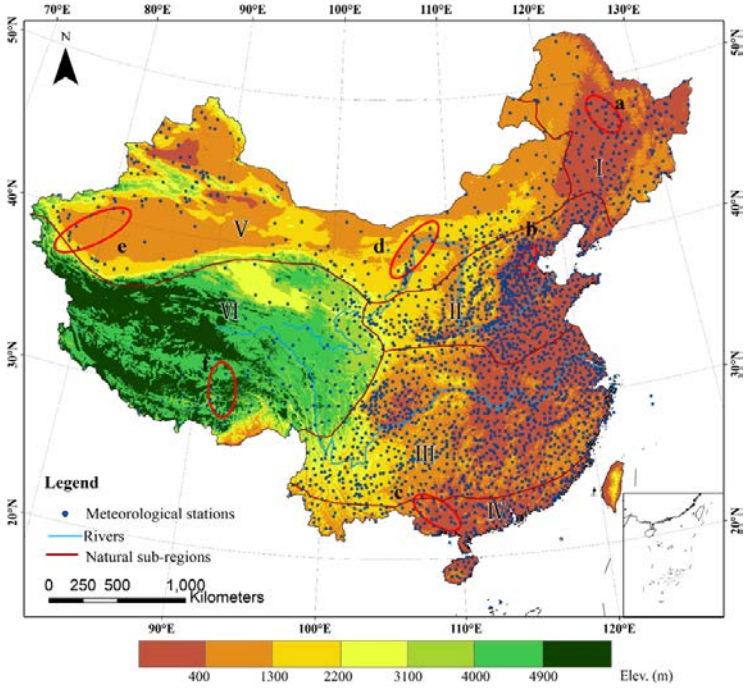

Figure 1: The study area divided into six natural subregions (I, II, III, IV, V, VI), and the spatial patterns of the meteorological stations in the subregions. The red circles mark the key areas where the temperature changes significantly, and these areas are used to validate the accuracy of the new LST dataset (a, b, c, d, e, f).

Table 1 Basic information for some of the meteorological stations in key zones

Region	key zone	ID	Latitude (°)	Longitude (°)	Altitude (m)
I Northeast Region	a	50758	47.10	125.54	249
I Northeast Region	a	50658	48.03	125.53	237
I Northeast Region	a	50756	47.26	126.58	239
I Northeast Region	a	50656	48.17	126.31	278

https://doi.org/10.5194/essd-2019-155
Preprint. Discussion started: 11 October 2019

I Northeast Region	a	50548	49.05	123.53	282
II North China Region	b	54525	117.28	39.73	5
II North China Region	b	54527	117.05	39.08	3
II North China Region	b	54518	116.39	39.17	8
II North China Region	b	54511	116.19	39.57	52
II North China Region	b	54624	117.21	38.22	7
II North China Region	b	54623	117.43	38.59	6
IV South China	c	59431	22.63	108.22	122
IV South China	c	59242	23.45	109.08	85
IV South China	c	59037	23.93	108.10	170
IV South China	c	59228	23.32	107.58	108
IV South China	c	59446	22.42	109.30	66
V Northwest Region	d	53336	41.40	108.48	1275
V Northwest Region	d	53446	40.34	109.50	1044
V Northwest Region	d	53602	38.52	105.34	1561
V Northwest Region	d	53513	40.48	107.30	1039
V Northwest Region	e	51730	40.33	81.19	1012
V Northwest Region	e	51716	39.48	78.34	1117
V Northwest Region	e	51810	38.56	77.40	1178
V Northwest Region	e	51811	38.26	77.16	1231
VI Qinghai-Tibet Plateau Region	f	55279	31.48	89.40	4700
VI Qinghai-Tibet Plateau Region	f	55591	29.42	91.08	3648
VI Qinghai-Tibet Plateau Region	f	55598	29.15	91.47	3560
VI Qinghai-Tibet Plateau Region	f	56106	31.53	93.48	4022

https://doi.org/10.5194/essd-2019-155
Preprint. Discussion started: 11 October 2019

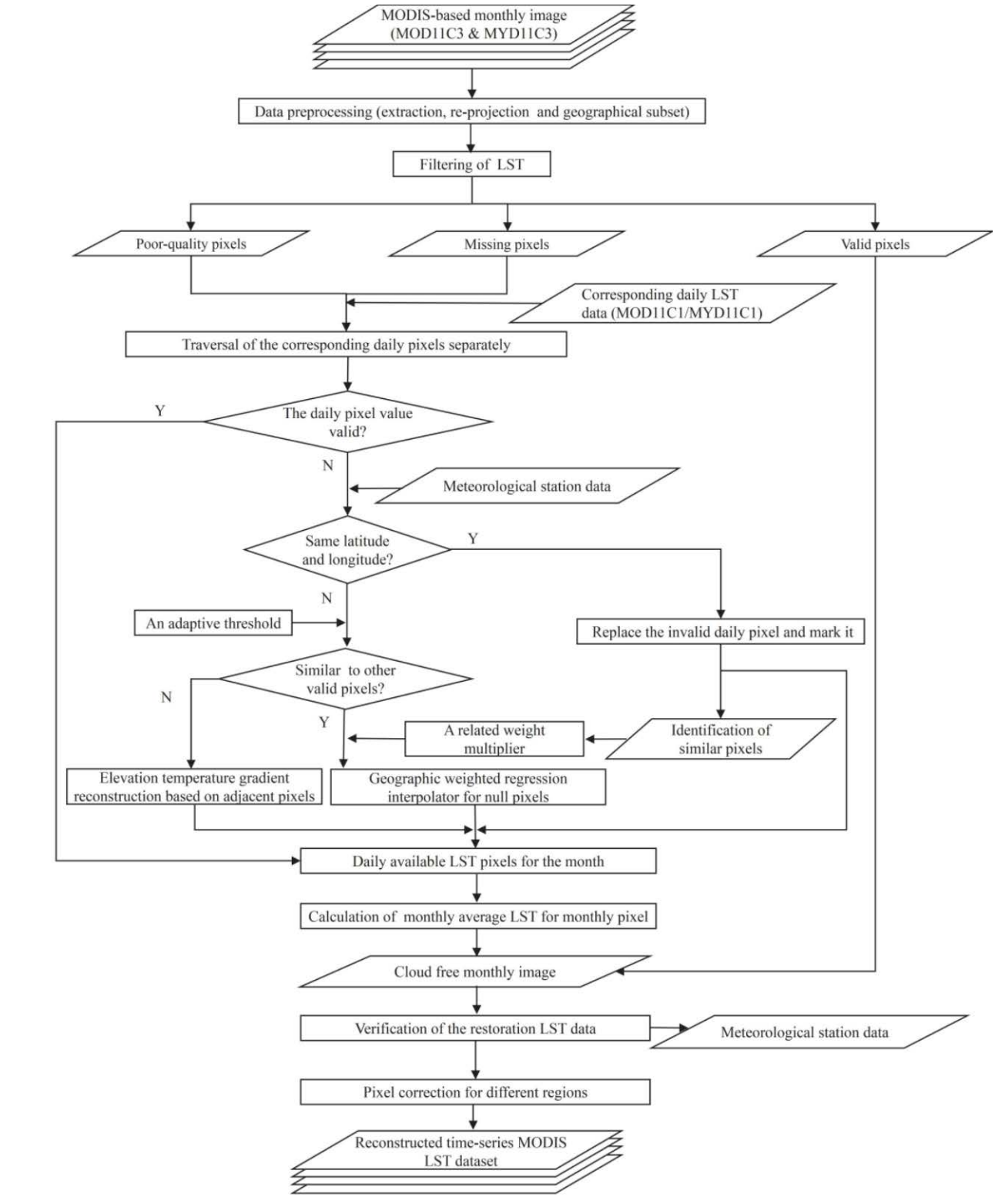

https://doi.org/10.5194/essd-2019-155
Preprint. Discussion started: 11 October 2019

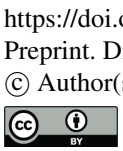

Open Access Earth System Science Data Discussions

Figure 2: The summary flowchart for reconstructing MODIS monthly LST data.

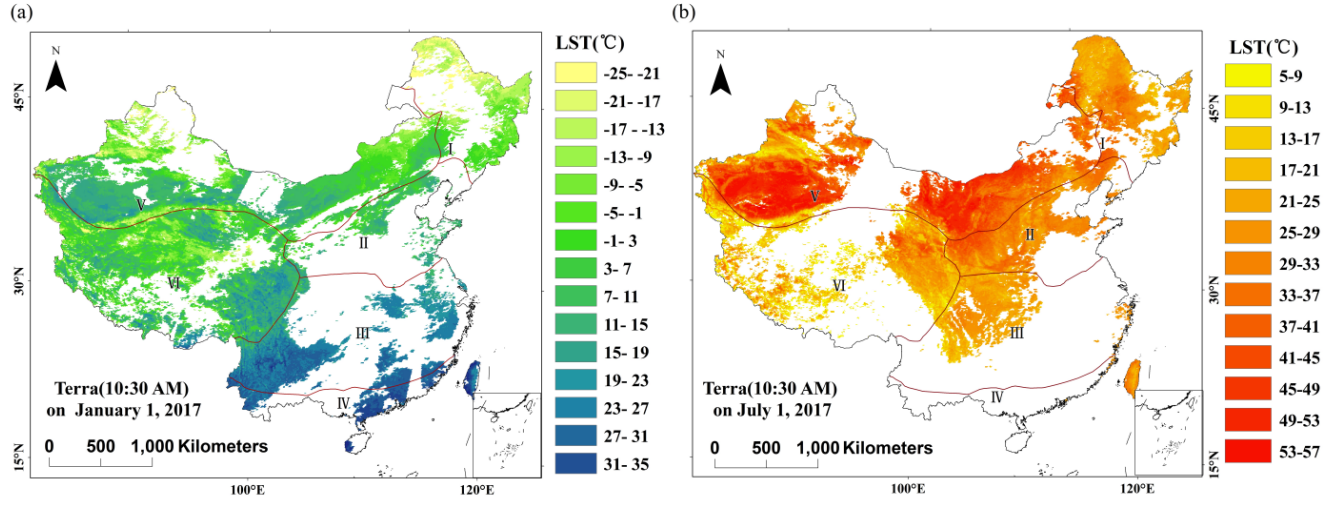

Figure 3: Spatial distribution of valid data for daily MODIS LST data from Terra at 10:30 am (a) January 1, 2017, and (b) July 1, 2017. Areas of invalid data are in white.

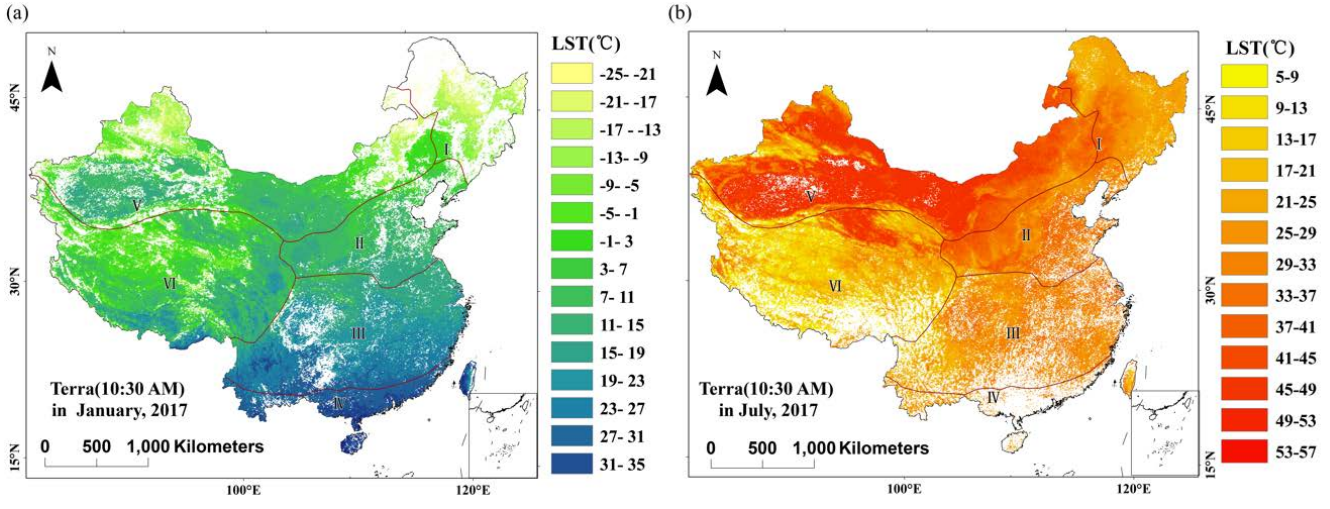

Figure 4: Spatial distribution of valid data for monthly MODIS LST data from Terra at 10:30 am in (a) January and (b) July. Areas of invalid data are in white.

https://doi.org/10.5194/essd-2019-155
Preprint. Discussion started: 11 October 2019

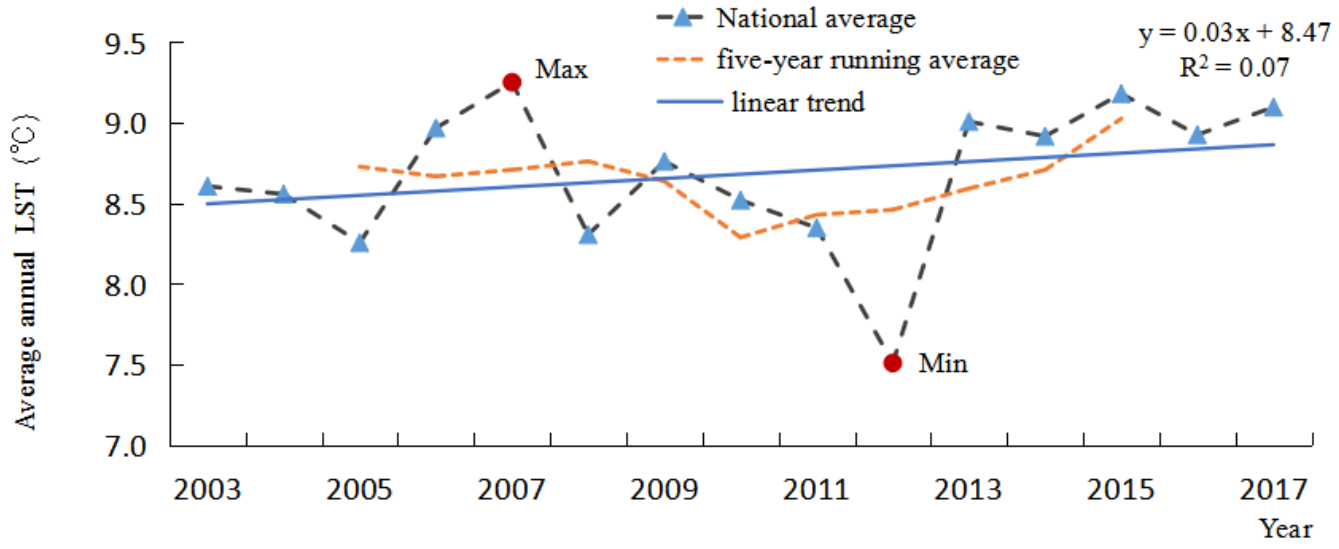

Figure 5: Annual mean LST changes in China from 2003 to 2017.

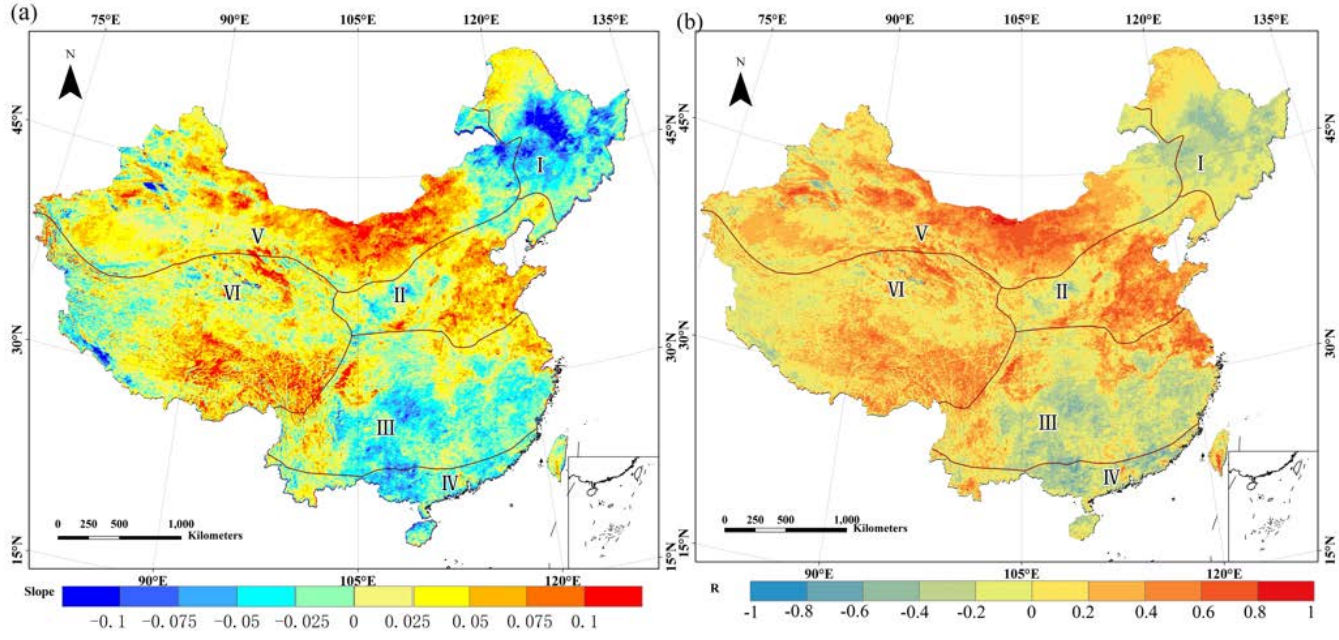

https://doi.org/10.5194/essd-2019-155
Preprint. Discussion started: 11 October 2019

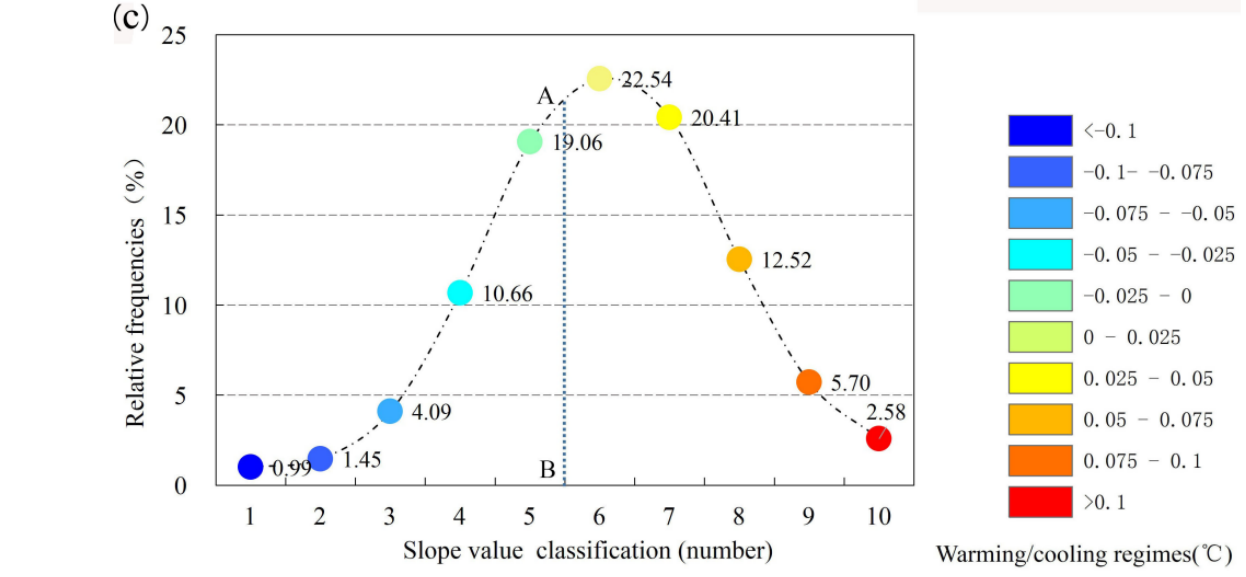

860

Figure 6: Spatial dynamics of interannual change trends in LST from the slope (a) computed by Eq. (8), the correlation coefficient (b) computed by Eq. (9) and frequency distribution of the slope (c) during 2003-2017. In panel c, the different temperature trends (slope) are divided into 10 subinterval ranges corresponding to the ranges in panel a. The left side of the AB line represents the proportion of the area that experienced cooling, and the right side represents the proportion that experienced warming.

865

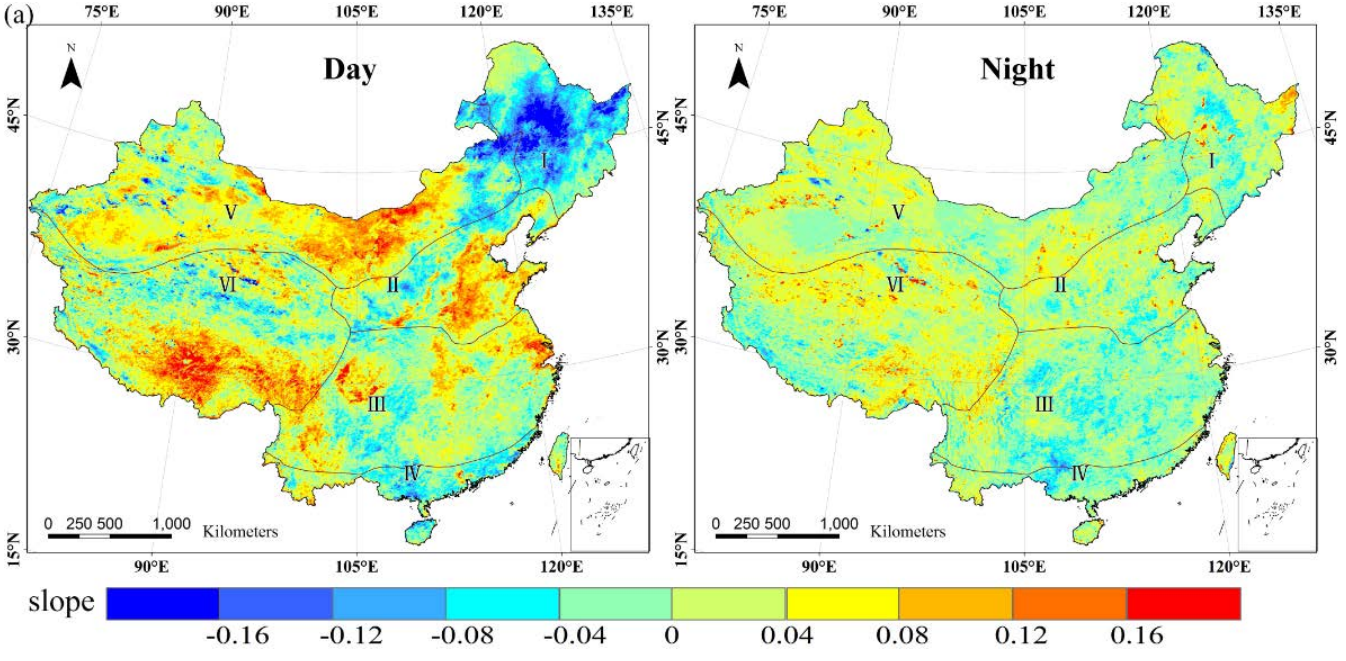

https://doi.org/10.5194/essd-2019-155
Preprint. Discussion started: 11 October 2019

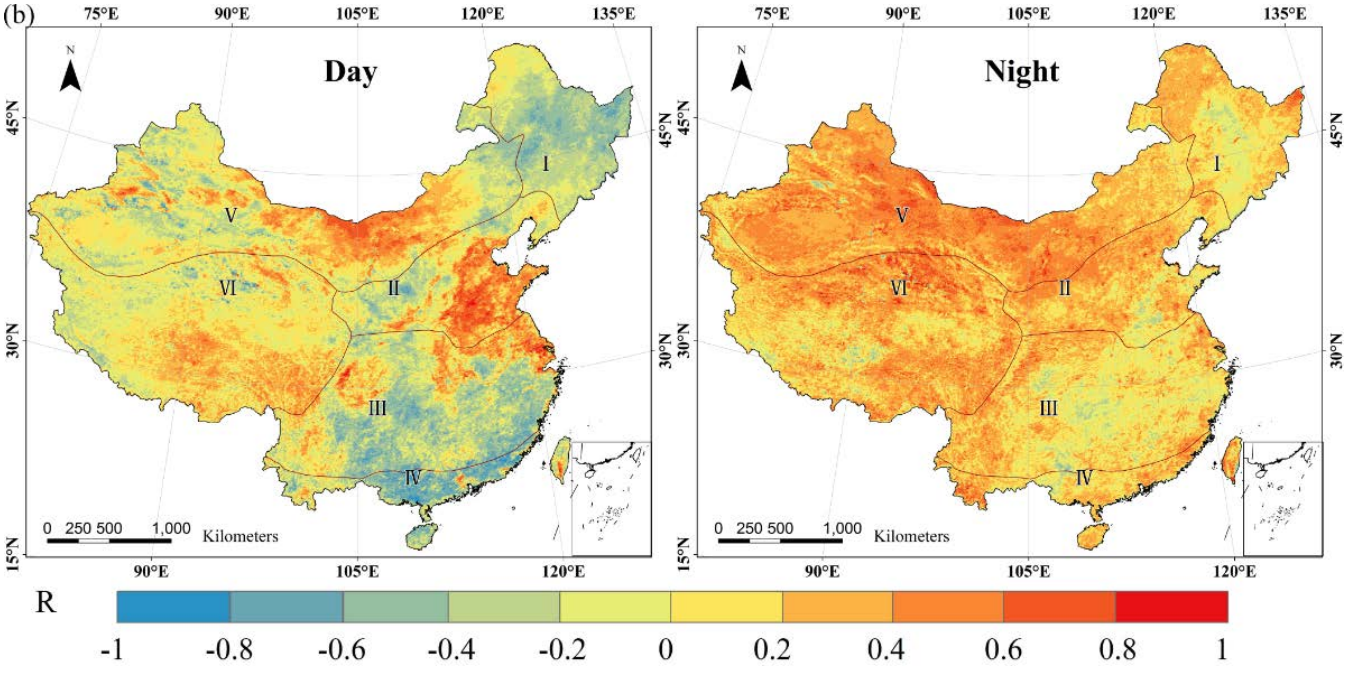

Figure 7: Spatial dynamics of interannual diurnal LST change trends from slope (a) and correlation coefficient (b).

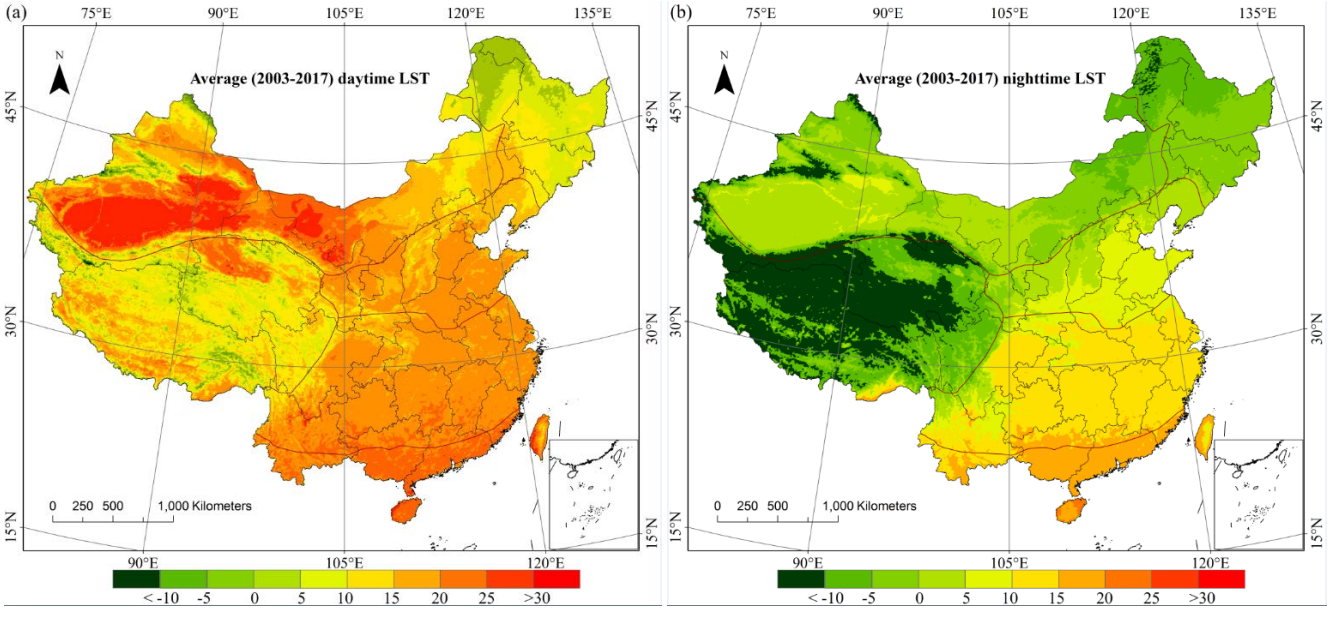

https://doi.org/10.5194/essd-2019-155
Preprint. Discussion started: 11 October 2019

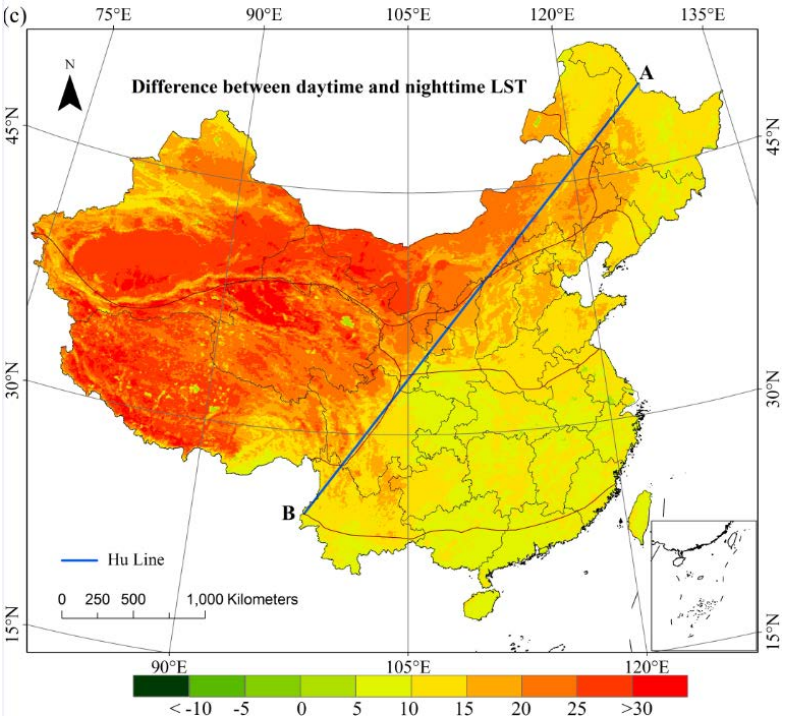

Figure 8: Spatial dynamics of average daytime LST (a), average nighttime LST (b) and difference between daytime and nighttime LST (c) from 2003 to 2017.

https://doi.org/10.5194/essd-2019-155
Preprint. Discussion started: 11 October 2019

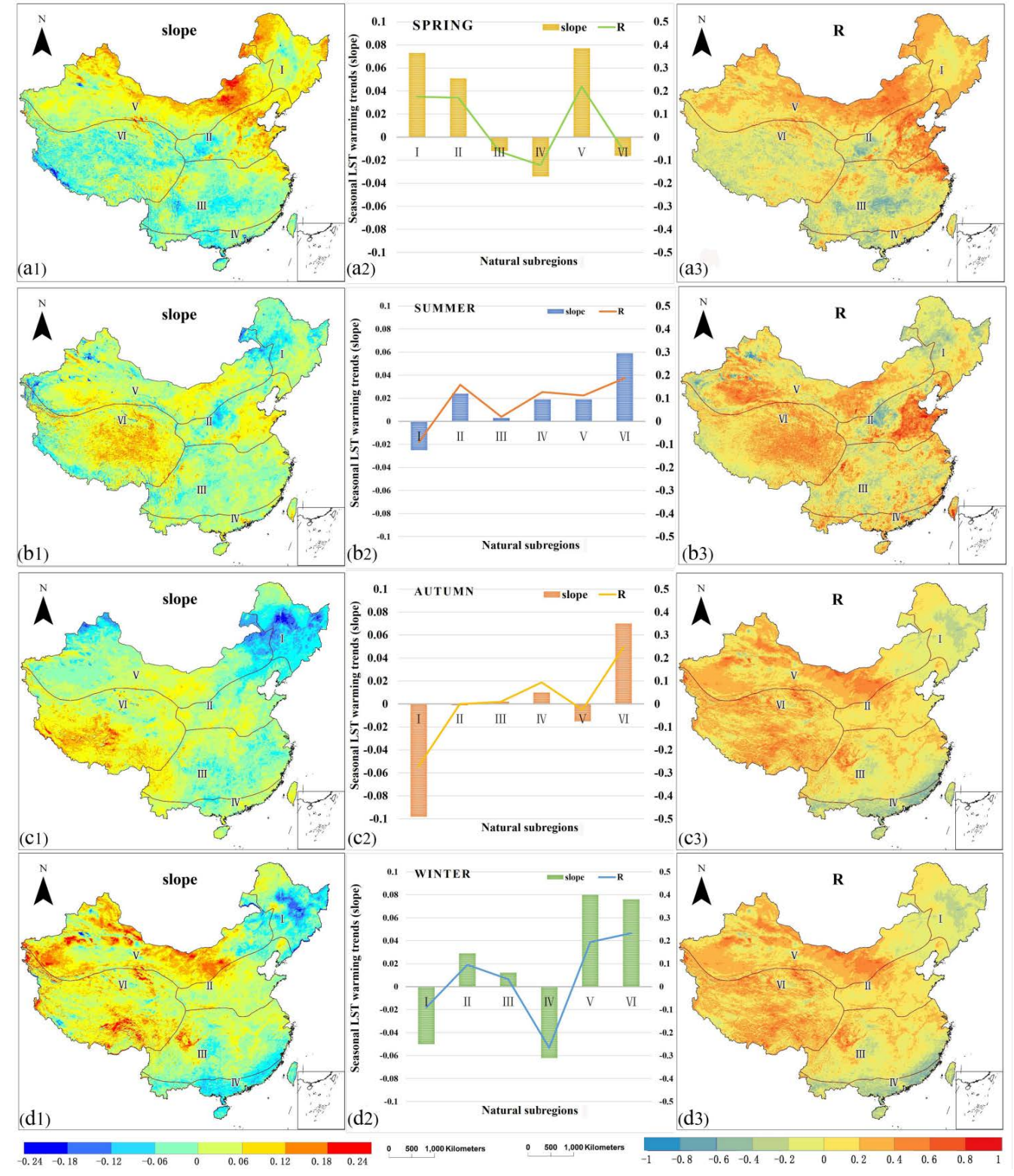

https://doi.org/10.5194/essd-2019-155
Preprint. Discussion started: 11 October 2019

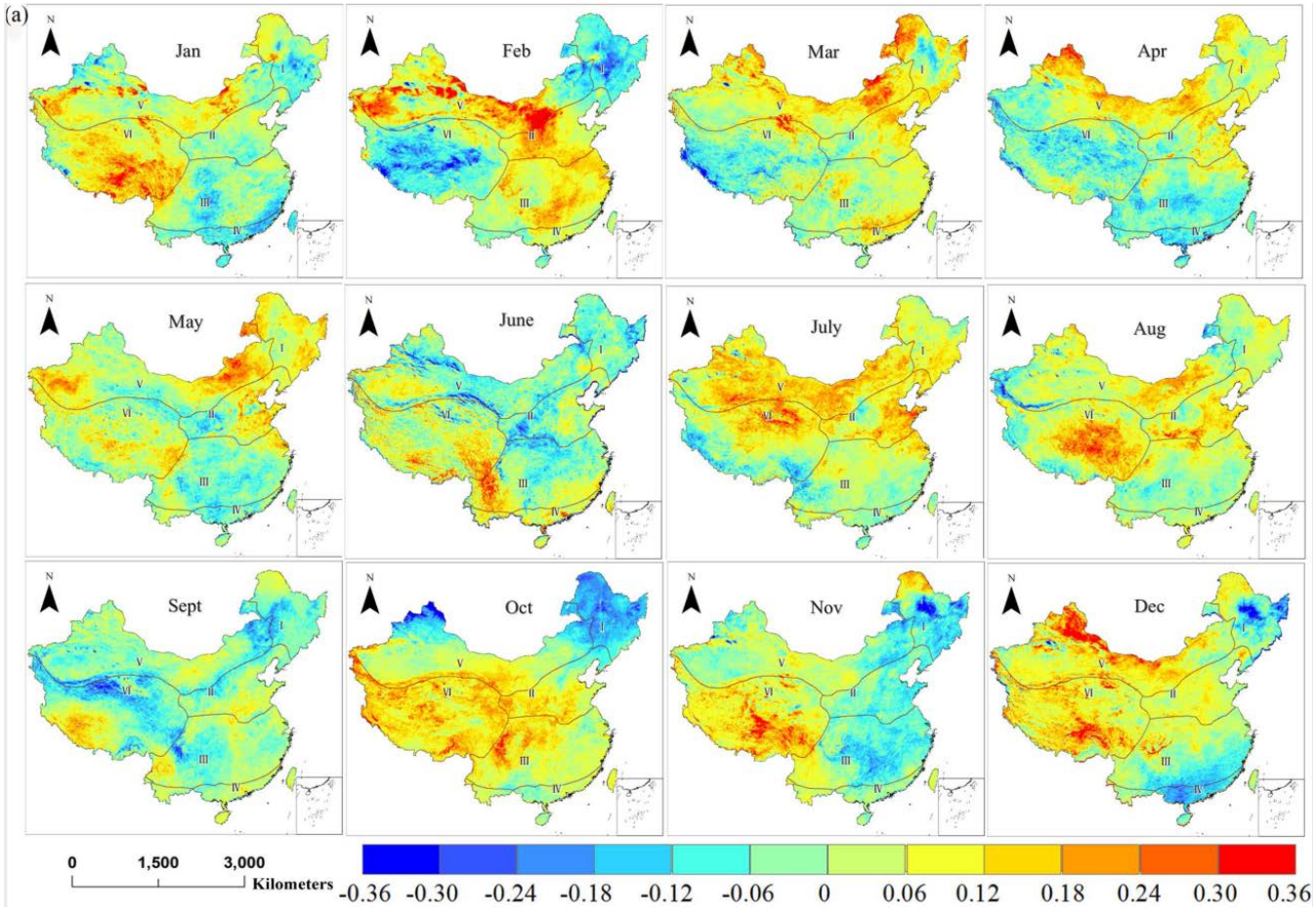

Figure 9: The interseasonal variability rates (slope) and correlation coefficients (R) of LST in spring (a), summer (b), autumn (c) and winter (d) from 2003 to 2017, a1, b1, c1 and d1 are the spatial distributions of the slopes at the four seasons, a2, b2, c2 and d2 are histograms of the slope of the four seasons, and a3, b3, c3 and d3 are the spatial distribution of the correlation coefficient (R) at the four seasons.

https://doi.org/10.5194/essd-2019-155
Preprint. Discussion started: 11 October 2019

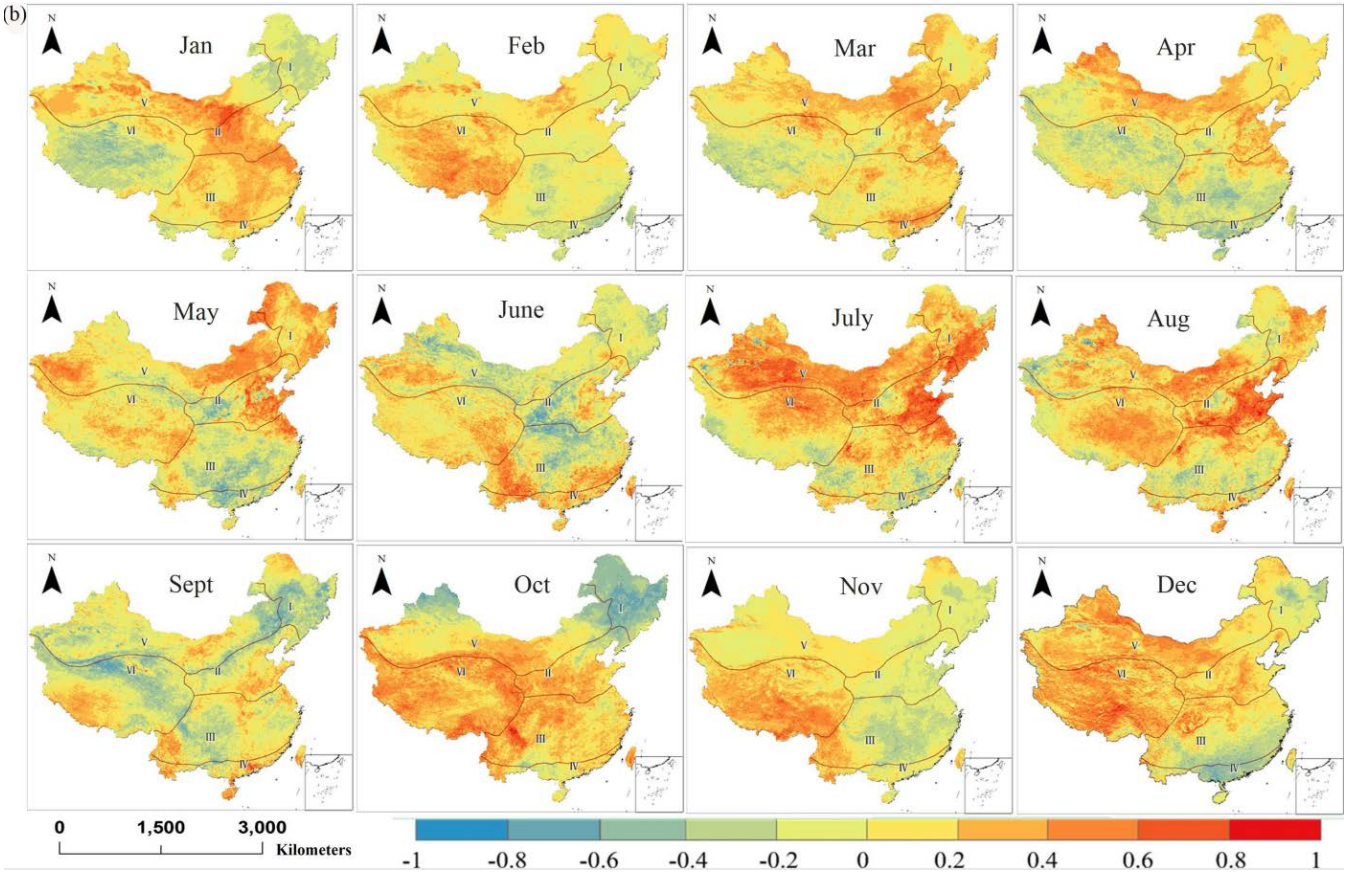

Figure 10: The monthly variability rates from slope (a) and correlation coefficients (b) of LST from 2003 to 2017.

https://doi.org/10.5194/essd-2019-155
Preprint. Discussion started: 11 October 2019

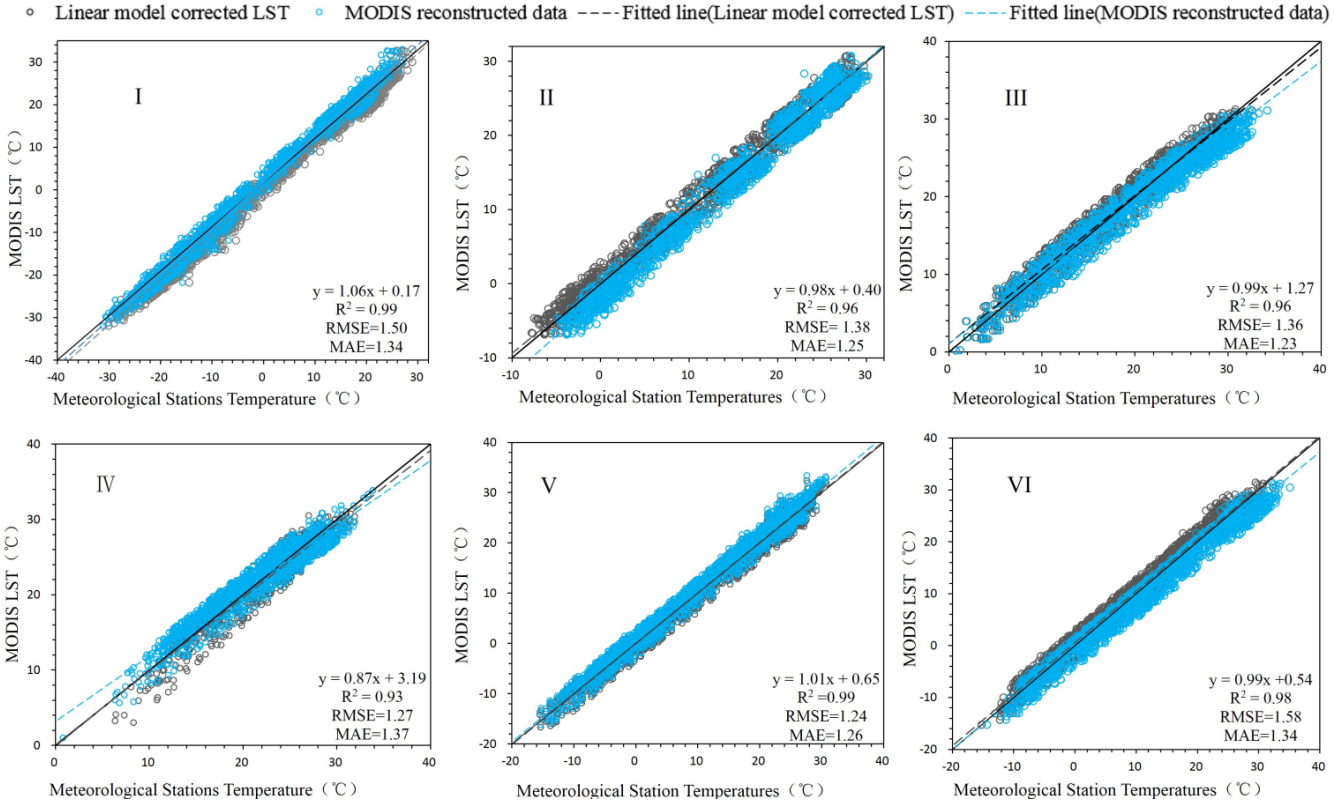

Figure 11: The scatter diagrams in six natural subregions (I, II, III, IV, V, VI) between the ground station data and the MODIS LST data. The blue scatter indicates the verification result of the reconstructed MODIS LST, and its statistical accuracy measures (R^2, RMSE, MAE) are also indicated. The result of the linear model corrected corrected is indicated in gray.

Table 2. RMSEs of seasonal LST between monthly LST (including the original LST and reconstructed LST) and ground-based LST (Orig. indicates the original LST located at ground stations. Recon. indicates the reconstructed LST located at ground stations)

Region	key zone	ID	Spring		Summer		Autumn		Winter	
			Orig.	Recon.	Orig.	Recon.	Orig.	Recon.	Orig.	Recon.
I Northeast Region	a	50758	2.11	1.48	1.36	1.23	1.16	0.61	3.80	3.81
I Northeast Region	a	50658	2.33	1.03	1.61	0.63	0.29	0.27	4.32	3.20
I Northeast Region	a	50756	3.51	0.23	1.03	0.43	0.51	0.26	3.91	3.52
I Northeast Region	a	50656	0.65	0.65	0.90	0.92	0.42	0.04	3.63	3.67
I Northeast Region	a	50548	0.82	0.89	1.09	0.61	0.51	0.40	0.15	0.15
II North China Region	b	54525	3.11	2.26	3.30	2.23	2.11	1.51	2.11	0.94
II North China Region	b	54527	1.30	1.11	1.24	1.25	0.93	0.54	2.36	0.14

https://doi.org/10.5194/essd-2019-155
Preprint. Discussion started: 11 October 2019

II North China Region	b	54518	3.64	1.64	0.52	0.51	0.45	0.15	0.71	0.04
II North China Region	b	54511	1.06	1.26	0.33	0.32	0.50	0.66	1.07	1.27
II North China Region	b	54624	1.99	1.55	1.15	0.49	0.84	0.33	0.40	0.46
II North China Region	b	54623	0.13	0.06	0.48	0.17	1.31	1.06	2.65	2.02
IV South China	c	59431	1.71	2.73	0.12	0.06	1.05	1.02	2.91	2.91
IV South China	c	59242	2.0	1.08	2.52	1.86	0.03	0.09	2.91	2.59
IV South China	c	59037	1.08	0.73	1.26	0.94	0.78	0.78	1.00	1.01
IV South China	c	59228	0.92	0.38	1.99	1.75	1.61	0.84	0.75	0.28
IV South China	c	59446	2.01	1.30	0.97	0.78	0.49	0.49	2.40	2.39
V Northwest Region	d	53336	3.88	3.88	3.04	3.04	3.53	2.81	1.90	1.82
V Northwest Region	d	53446	2.00	2.01	3.78	3.18	1.96	1.65	0.35	0.35
V Northwest Region	d	53602	4.48	4.28	3.91	3.75	3.97	3.47	1.65	1.65
V Northwest Region	d	53513	1.55	1.48	5.33	5.15	5.01	4.93	2.04	2.24
V Northwest Region	e	51730	3.01	2.97	4.09	5.08	1.48	1.06	2.63	2.10
V Northwest Region	e	51716	0.80	0.75	0.47	0.15	0.74	0.09	0.66	0.32
V Northwest Region	e	51810	2.33	1.29	1.20	0.76	0.33	0.32	1.24	0.28
V Northwest Region	e	51811	0.57	0.57	0.52	0.90	0.62	0.36	1.34	0.39
VI Qinghai-Tibet Plateau Region	f	55279	3.63	3.44	1.37	1.74	1.83	1.45	0.99	0.99
VI Qinghai-Tibet Plateau Region	f	55591	1.76	1.79	5.56	4.08	2.99	2.59	1.95	0.41
VI Qinghai-Tibet Plateau Region	f	55598	0.85	0.85	4.37	4.62	2.95	2.91	0.63	0.69
VI Qinghai-Tibet Plateau Region	f	56106	0.52	0.58	1.44	1.44	0.88	0.68	2.11	1.99
Average			1.92	1.51	1.96	1.72	1.40	1.12	1.88	1.49